CMB-S4 DETECTOR DEVELOPMENT & SPT AGN MONITORING SYSTEM

By

John Calven Hood II

Dissertation

Submitted to the Faculty of the

Graduate School of Vanderbilt University

in partial fulfillment of the requirements

for the degree of

DOCTOR OF PHILOSOPHY

in

Astrophysics

December 17, 2022

Nashville, Tennessee

Approved:

Kelly Holley-Bockelmann Ph.D.

Stephan Meyer Ph.D.

Andreas Berlind Ph.D.

C.R O'Dell Ph.D.

Steven Padin Ph.D

David Weintraub Ph.D.

Copyright © 2022 John Calven Hood II
All Rights Reserved

I would like to dedicate this thesis to my village, hidden in the leaves. To the people that took me in and treated me like family and believed in me when I didn't believe in myself. This includes all of my close friends and family that have supported me throughout my journey and who, without a doubt, will be there with me for the remainder.

ACKNOWLEDGMENTS

First off, I am thankful for all the support and supervision from my advisor, Dr. Kelly Holey-Bockelmann. This work would not have been possible without her constant encouragement, mentorship, and guidance through all these years. I am grateful for all of the opportunities that I have been afforded during my time as a student at Vanderbilt. I am additionally beyond grateful for all of her help to find the right fit for me research-wise, eventually helping me find my way to Chicago. This has had a tremendous impact on my professional and personal life.

I am also grateful to the members of my committee for taking time from their busy schedules to help me along this journey. I am also grateful to my collaborators and advisors for all of their helpful suggestions, discussions, and advice over the past few years. I would like to thank my friends from both Vanderbilt and the University of Chicago and the SPT collaboration for their support and friendship. My time in graduate school would not have been the same without them. I am also grateful to all of my family in +BRD who have always been there to pick me up when I was down and motivate me to do my absolute best while pushing forward.

I would also like to thank my village for their endless support and constant encouragement throughout these years. Especially for Dr. C, who convinced me to change my major to astrophysics and has served as a supportive father figure for me throughout my entire academic career, and Dr. Cross, who, even though he wanted me to study biology since high school, pushed me to follow my chosen path and do what I loved.

Finally, I would also like to thank Tracey Hood for being there for me, especially during those times that I was writing the papers and applying for fellowships. For all the study breaks, for her patience and constant encouragement over the past 13 years of schooling, and for her companionship that has kept me going, especially in the final stretch of grad school. I am extremely grateful to her for always being there for me when I needed her and for keeping me grounded all these years. She has truly made a difference in my life, and for that I'm extremely grateful.

To all of my friends, family and loved ones, Thank you for helping me find the strength to change the narrative!

Figure 1: +BRD family crest

TABLE OF CONTENTS

LIST OF TABLES

LIST OF FIGURES

CHAPTER 1

INTRODUCTION

Observations of the Cosmic Microwave Background (CMB) provide a corner stone of our understanding of the universe, and recent and upcoming CMB experiments are measuring the millimeter-wave sky with ever increasing sensitivity. Furthermore, observations of the CMB are beginning to be used as more than just a tool to enrich our understanding of cosmology. In this thesis, I describe both methods that are being implemented to increase CMB detector sensitivity and how instruments like the South Pole Telescope (SPT) are now using novel astronomy techniques to monitor Active Galactic Nuclei (AGN), opening a new window of understanding these sources.

1.1 Time Domain Astronomy with SPT

From 2013 - 2016 SPTpol was used to survey 500 $\deg^2$ of the southern extragalactic sky at arc minute resolution to milli-Jansky levels. The survey consists of $\sim$3500 observations over $\sim$9000 hours at high Galactic latitude, covering 22^h to 2^h in right ascension and -65° to -50° in declination (Henning et al., 2018). This survey enables the monitoring of tens of mm-bright AGN on timescales from years to days at high S/N (> 10 in a 36-hour coadd). The observations provide the opportunity to include mm-band AGN variability monitoring in the study of the physical mechanisms of AGN emission regions and the physics of the energy source. Figures 1.1 and 1.2 show the difference between the typical maps used to study the CMB and a map that has been filtered to remove the CMB while keeping point sources. The filtering process performed in my study is described in greater detail in section 2.3.3.

1.2 Active Galactic Nuclei

Active Galactic Nuclei (AGN) are galaxies with actively accreting supermassive ($10^5 < M_\odot < 10^9$) black holes that are commonly found at the centers of massive galaxies (Kormendy and Richstone, 1995; Gebhardt et al., 2000; Carroll and Ostlie, 2007). As illustrated in Figure 1.3, a unified model of AGN can be used to explain all observed categories of AGN with a single physical picture.[1] For example, in this scenario, blazars—radio-loud AGN[2] that also emit strongly in the γ-ray band—are understood to have a relativistic jet pointed at relatively small angles (<5 deg) with respect to the line of sight of the observer (Antonucci, 1993; Urry and Padovani, 1995).

Blazars, and AGN in general, can be studied by using multi-wavelength observations from a wide array of instruments that range from radio telescopes to γ-ray telescopes. Radio observations can detect synchrotron

[1] The unified model of AGN is outdated.

[2] Radio loud AGN are generally defined as AGN with a ratio of radio (5 GHz) to optical (B-band) flux ≥ 10 (Kellermann et al., 1989).

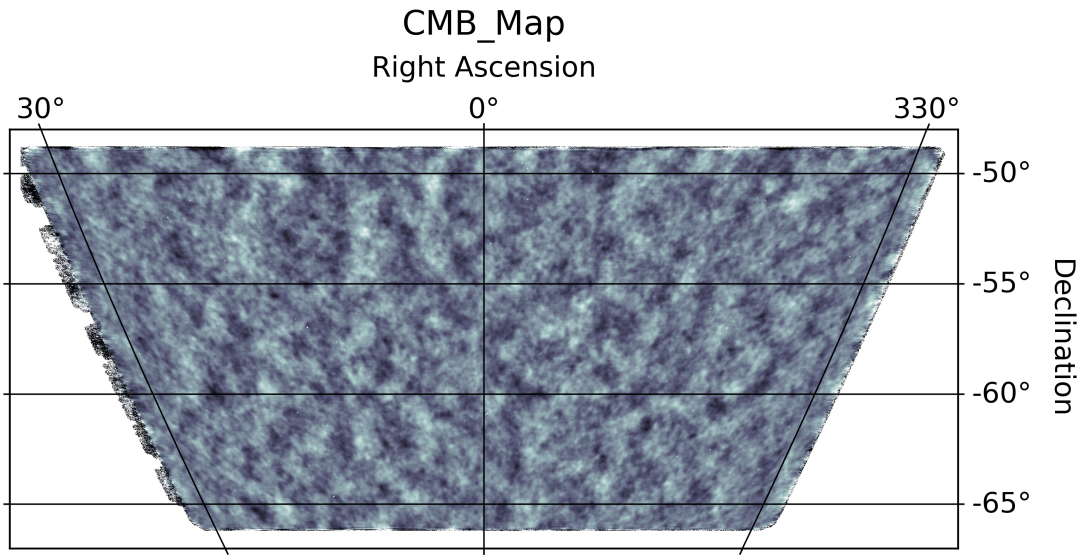

Figure 1.1: Unfiltered CMB survey map coadd.

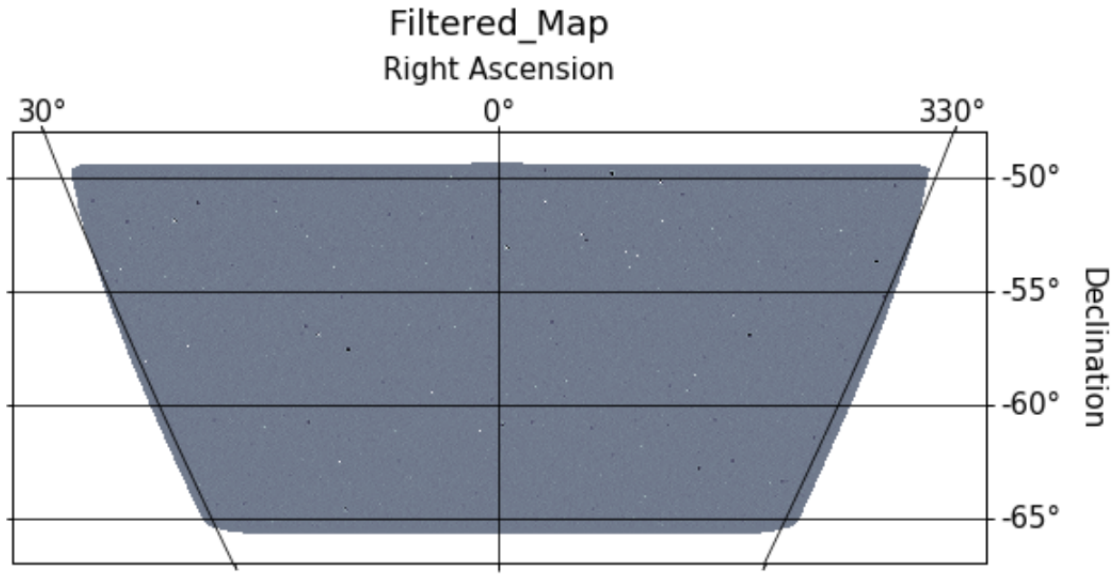

Figure 1.2: Matched filtered survey map coadd.

radiation, caused by accelerating charged particles in a magnetic field. On the other end of the electromagnetic spectrum in the high energy regime are γ-rays, the source of which is still under debate. A key input in the investigation of the origin of the γ-ray emission in blazars is the multi-wavelength study of blazars, particularly of blazar variability and flaring states. Such studies have traditionally included γ-ray, X-ray, optical, infrared, and radio emission. I have developed a systematic program designed to fill a gap in traditional AGN variability studies with a novel use of CMB data: turning CMB experiments into AGN monitors to study

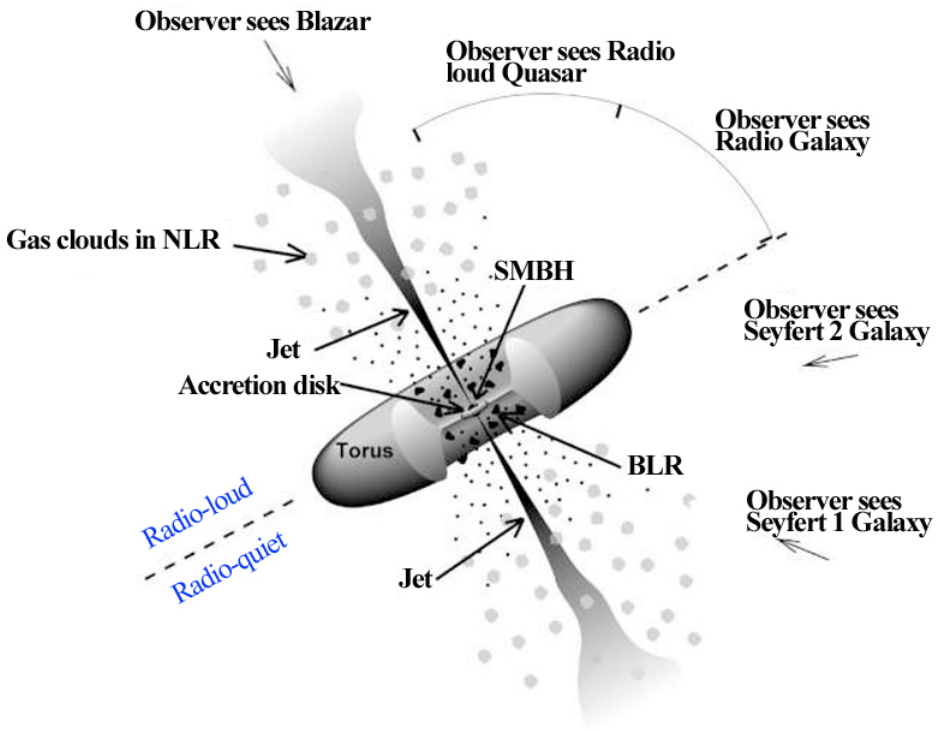

Figure 1.3: This diagram shows the Unified Model of AGN. The model attributes the wide range of observational signatures of various AGN types to a single type of object – an accreting supermassive black hole (SMBH). The lower half of the diagram represents the radio-quiet class, while the top represents the radio-loud class. This research focuses on the latter classification. Depicted here is a SMBH surrounded by an accretion disk and a dusty torus. Depending on the angle of the observer's line of sight, they may either observe a radio galaxy (observed along the axis of the torus), a radio-loud quasar (observed between 45 and 80 degrees above the torus axis) or a blazar (observed between 80 and 90 degrees above the torus axis). The latter is a scenario where the observer is looking down the jet of the AGN. Image courtesy NASA and Fermi.

them in the millimeter waveband.

In this thesis, I will provide evidence that the addition of high-cadence, long-timescale mm-wave AGN monitoring—made possible by re-purposing CMB data—will shed light on many of the key questions in blazar studies.

As shown in Figure 1.4, the spectral energy distribution (SED) of blazars has a characteristic double-humped structure, with one peak (anywhere from the radio to the X-ray band) caused by synchrotron emission from energetic electrons in the blazar jet, and a high-energy peak in the MeV-TeV γ-ray band (Fossati et al., 1998). Attempts to explain this double-humped structure can be divided into two classes of models that invoke three different physical mechanisms. These models are the hadronic and leptonic models: In the hadronic model, processes such as photo-pion production produce the TeV peak, while in the leptonic models, that peak is caused by inverse-Compton scattering of lower-energy photons. These lower-energy photons can be

the same synchrotron photons responsible for the low-energy peak (the "synchrotron self-Compton" model) or other components of the radiation field (the "external inverse-Compton" model).

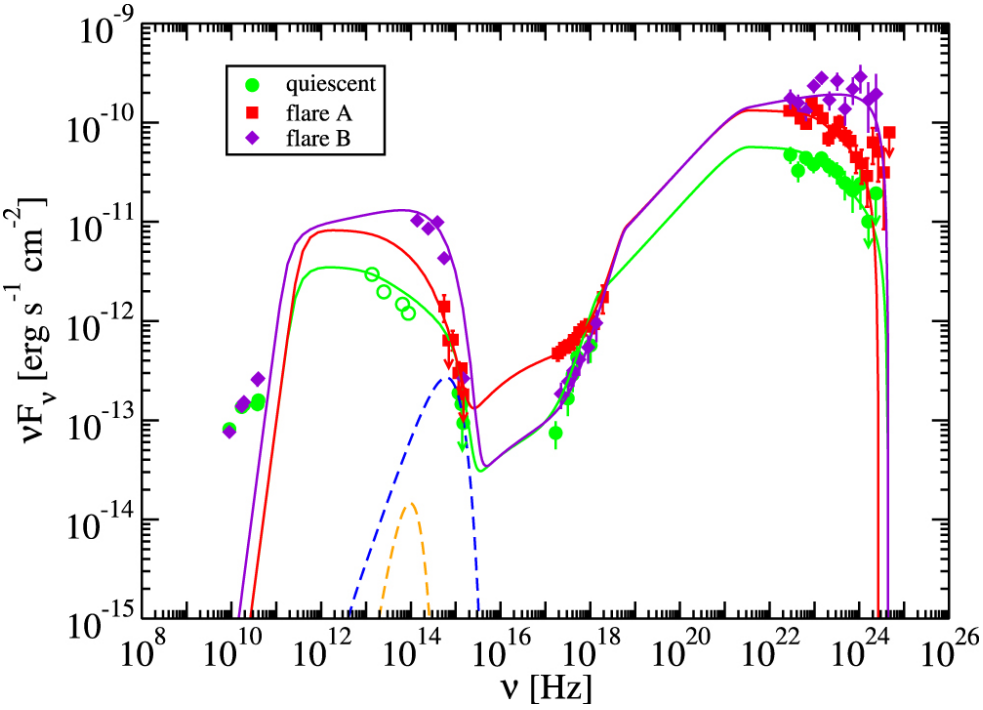

Figure 1.4: Broadband SED model for PKS 2326-502. The data are modeled with a one-zone leptonic model of blazar emission (Finke et al., 2008). The low-energy component is modeled as a combination of synchrotron emission from the jet and thermal emission from the accretion disk. A double broken power law is used to model the electron distribution during the quiescent state flare A. A change in the size of the emitting region is used to model flare B. The smaller dashed yellow-orange curve represents emission from the dust torus and the larger dashed blue curve is accretion disk emission. The high-energy component is explained by inverse Compton scattering of dust torus photons by electrons within the jet. Hollow circles represent non-simultaneous data. Figure reproduced from Dutka et al. (2017).

CHAPTER 2

SOUTH POLE TELESCOPE

2.1 Background

The South Pole Telescope (SPT, see Figure 2.1) is a 10 m millimeter-wavelength telescope located at the NSF Amundsen-Scott South Pole Station in Antarctica, originally built to study the CMB via continuous dedicated observations. The SPT is able to observe the sky with arcminute resolution at 150 GHz with a square degree field of view. The south pole location was chosen because it is a dry desert (very little water vapor to absorb the mm-wave radiation) located at a very high altitude of 9300 ft or $\sim$2800 m. At this high altitude, the atmosphere is very stable and much thinner, resulting in more radiation being able to reach the detectors and more importantly, lower sky noise. The high stability of the atmosphere is due to the sun rising and setting only once a year, providing no daily heating and cooling.

Figure 2.1: South Pole Telescope and the moon. Image courtesy of Daniel Luong-Van.

To date, three different cameras have been installed on the SPT. The first camera, SPT-SZ, was installed in 2007 and is only sensitive to temperature fluctuations and not polarization. SPT-SZ was actively observing between 2007 and 2011 and primarily surveyed a 2500 deg^2 field with detectors sensitive to radiation in bands centered at 95, 150, and 220 GHz (Story et al., 2013) which are in spectral windows of high atmospheric transmission. The second generation camera was the SPTpol. SPTpol was installed in 2012 with polarization

sensitive detectors sensitive to radiation in bands centered at 95 and 150 GHz and was actively observing between 2012 and 2016. This thesis uses data from this camera. The SPTpol instrument was capable of both temperature and polarization measurements of the CMB. This camera consists of 180 polarization sensitive pixels at 90 GHz that are coupled by feedhorn arrays that surround the seven hexagonal sections of 150 GHz detector modules (Henning et al., 2012) as seen in Figure 2.2. The most recent receiver being used is SPT-3G (Sobrin et al., 2022), which was deployed in 2017 and has 2700 multichroic pixels sensitive to radiation in bands centered at 95, 150, and 220 GHz and 2 polarizations, for a total of 16200 detectors.

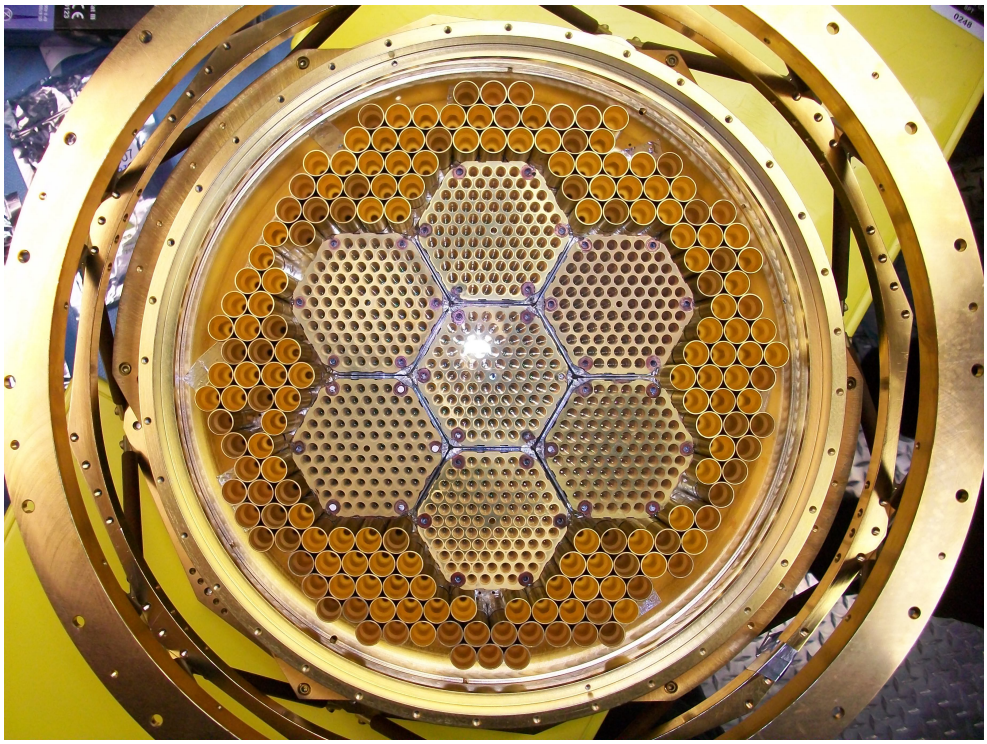

Figure 2.2: SPTpol focal plane. Image courtesy of Brad Benson.

2.2 500 square degree survey

The 500 $\deg^2$ SPTpol survey consists of $\sim$3500 observations over $\sim$9000 hours at high Galactic latitude, covering 22^h to 2^h in right ascension and -65° to -50° in declination as seen in Figure 2.3. One observation of the survey field consists of either 106 or 109 constant-elevation raster scans, depending on the observing strategy discussed below, with the telescope first scanning right and then left. After each right-to-left scan pair, the telescope makes a step in elevation of either 9.2' or 9.0' before making another set of paired scans.

This process repeats until the field is completely mapped once, and we define this set of scans as a single observation. Between 2012 and 2016, two different observing strategies were used. From first light in 2012 through May 2014, a lead-trail strategy was used, and from then on, a full field strategy was used (Henning

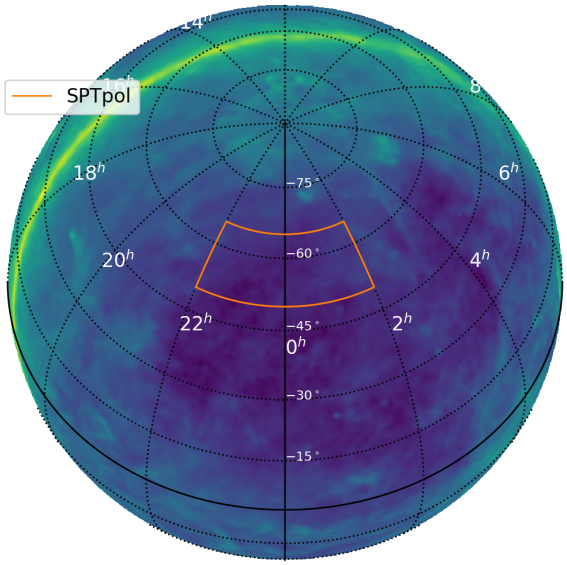

Figure 2.3: Orthographic projection of the SPTpol 500 deg^2 survey field, where the background is the Planck dust map (Planck Collaboration et al., 2014).

et al., 2018). For lead-trail observations, the field is split into ”lead” and ”trail” halves, which are forced to match in azimuth for removal of ground contamination. For the full field strategy, we scanned the entire R.A. range of the field.

2.3 Data Selection and Analysis Procedure

The following section will explain the methods and techniques used in order to conduct the pilot study described in Chapter 3. This pilot study is the first large-scale effort to use CMB data for AGN monitoring and will provide a foundational observing program/strategy that will be implemented in future CMB experiments. In order to use CMB observations to monitor AGN, we first needed to produce the maps necessary to conduct millimeter wavelength photometry on our selected sources. Each map was produced by combining a number of single observations over a 36 hour period into bundles for Signal-to-Noise purposes.

2.3.1 Map selection

As mentioned in Section 2.2, the SPTpol survey during its time on the sky was able to take a large number of observations. With the observing strategy outlined previously, the SPTpol survey scanned the entire survey field and made 1 map every 2 hours, producing 12 total maps per full day of observing.

Before making our map bundles, the standard deviation using the signal for the brightest point source in the field for the full coadd was found and calibrated to milli-Janskys(mJy). That conversion was done using

the following variables and equations:

$$x = \frac{h}{k_b}\frac{\nu}{\mathrm{Tcmb}}, \tag{2.1}$$

where Tcmb = 2.725 K, c = 2.9979×10^8 m/s, h = 6.62607×10^{-34} J/s, k_b = 1.38065×10^{-23} J/K and frequency = 150×10^9 Hz. We also calculate the beamsize (Ψ) in radians with:

$$\Psi = \frac{\Theta_{\mathrm{F}}}{60}\frac{\pi}{180}, \tag{2.2}$$

where Θ_F is the Full Width Half Maximum input equal to 1 arcminute to reflect the SPTpol instruments beam on sky. Ω_b is calculated by using Ψ in arcminutes:

$$\Omega_b = \frac{\pi}{4\log 2}\Psi^2, \tag{2.3}$$

We also calculate Ξ, which is a necessary prefactor needed to make the conversion that includes everything but frequency dependence and the beam using the same physical constants mentioned before:

$$\Xi = 2.0k_b(\frac{b\mathrm{Tcmb}}{hc})^2. \tag{2.4}$$

We then can plug all of these variables into:

$$\frac{\mathrm{mJy}}{\mu K} = \frac{1 \times 10^{29}}{1 \times 10^6}\frac{\Xi\Omega_b e^x x^4}{(e^x - 1.0)^2}, \tag{2.5}$$

This final equation allows us to convert our flux from μKelvin to milliJansky. This conversion leads us to measuring a full coadd σ of 10.89 μK which, when converted to flux using equation 2.5, leads to a 1σ flux uncertainty of 0.635 mJy. Then, we use fluxes from the SPTpol source list to figure out the expected S/N, using Equation 2.6 below.

$$\frac{S}{N} = \frac{\mathrm{F}}{\sigma_{mJy}}. \tag{2.6}$$

With an expected S/N now determined, we then needed to decide on the best cadence necessary to conduct our AGN monitoring program.

2.3.2 Bundling Maps

In order to settle on the best cadence, we first checked other AGN monitoring programs to determine their cadence. We found that there was a range that was between daily and weekly monitoring between the optical

SMARTS survey (Bonning et al., 2012) and the Fermi γ-ray survey (Abdollahi et al., 2020). After reviewing the cadence of the Fermi and SMARTS data, we designed our bundle maps by combining an average of 10 maps per bundle, which is roughly 36 hours. These 36-hour bundles provide us with an expected S/N of 10 or greater for the top 20 brightest sources found in the survey field via the coadd calculations. These bundled maps must now be filtered to remove the CMB and other long-spatial wavelength features to permit flux extraction.

2.3.3 Matched Filtering

The filtering method we used was a matched filter. The matched filter suppresses angular scales on which the S/N on a point source is low and maximizes the total S/N on point sources in a map. The signal used in our matched filtering requires a number of variable inputs that include the point source profile that describes the signal we are looking for. After each map was matched filtered, additional tests were implemented to look for possible systematic errors. The first test was a calibration check. In this check, for each map of ours, the average ratio of two power spectra in the ell range [750, 1250] is calculated; the numerator is the spectrum of the cross-correlation between our map and Planck's full-mission T map, and the denominator is the cross-spectrum between Planck's two half-mission T maps. For the ell bin width, I used the same value as in the case of the noise level calculation (50). If our temperature calibration is reasonably close (0.9 or above) to that of Planck's, this ratio should be close to 1.0. These calibration ratios were applied to each map in order to correct source fluxes. The next test we implemented was a pointing test. In this test, we ran an astrometry check which that matched the RA and DEC of sources found in our map to the positions in the Australia Telescope 20 GHz (AT20G) catalog (Murphy et al., 2010a).

To test the filtering process, we first applied the matched filter and calibrations to our full coadd CMB map. In these maps we can easily see the typical CMB patches and structures, but if we zoom in, as seen in Figure 2.4, we can see that there are point sources visible but sitting on the CMB fluctuations in the unfiltered maps. After filtering, we get maps where we can see that the typical CMB patches and structures have been largely removed. In some spots, we can even start to see where some of the really bright sources will be found. When we zoom here in Figure 2.5, we can see that the filtering has worked well as we see the bright point sources as bright dots with dark rings around them, which is an artifact from the filtering process.

Using the filtered maps, we search for the AGN in the field. As a further check, we plot light curves for the top 15 brightest objects on our point source list, as seen in Figure 2.6, and inspect these curves for any obvious correlated structure that would indicate instrumental systematics. We see no evidence of similar behaviors between any of the light curves, which indicates that any fluctuations seen in the light curves are intrinsic to the sources themselves.

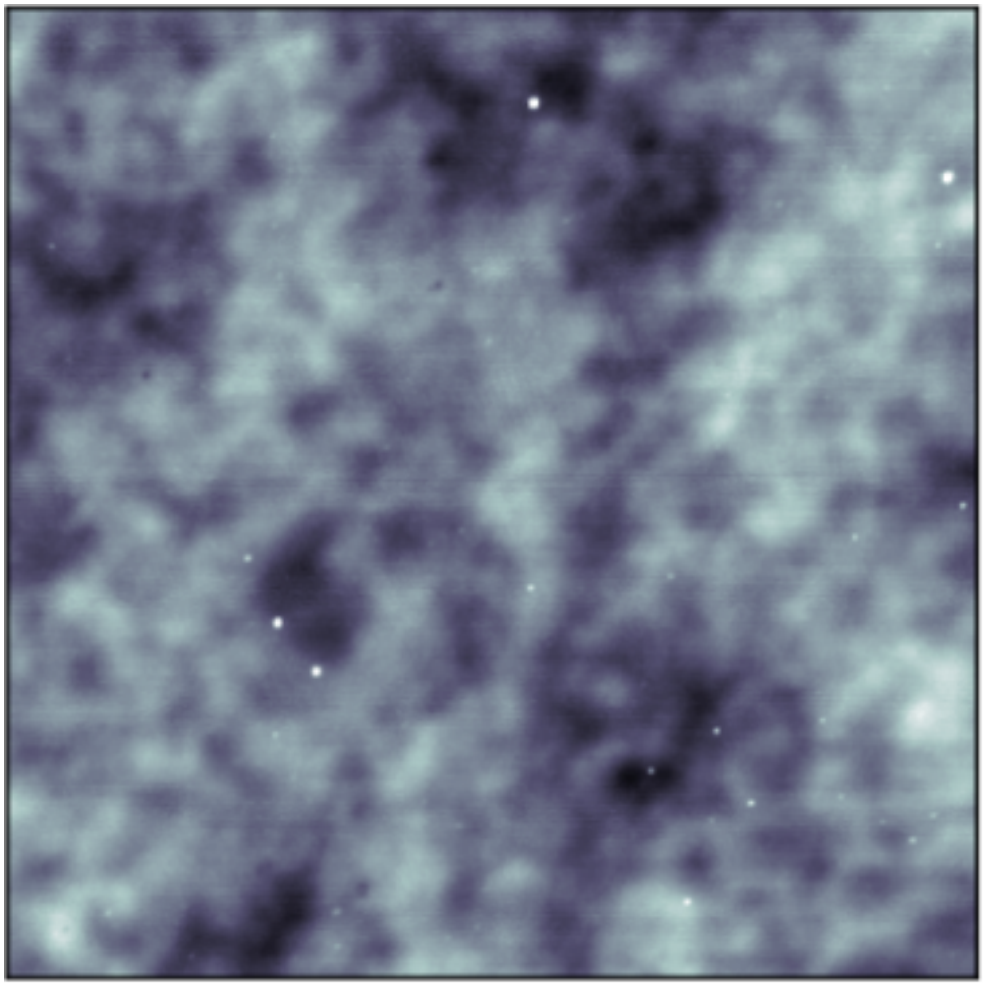

Figure 2.4: 5 x 5 degree section of unfiltered CMB map.

2.3.4 Source Selection

The product we look to build in this section is a list of AGN found in the SPTpol 500 $\deg^2$ survey field that we could possibly monitor. To do this, we looked thorough the SPT-SZ point source catalog published in Everett et al. (2018). This survey covered a larger 2500 $\deg^2$ field, of which, our 500 $\deg^2$ field was a subset. We began by identifying all of the bright point sources found in the SPT catalog using a very broad definition of locations near the 500 $\deg^2$ footprint and made thumbnails to find sources that were within the RA and DEC bounds of the survey. These locations were used to identify point sources by taking snapshots of a 20 x 20 pixel area around the locations to check if each location was within the survey field and not on the outer edges as seen in Figure 2.7. In this figure we see that some snapshots contain bright point sources while others contain blurs. These blurs are due to the coordinates being outside of the bounds of the actual survey field. These points were later excluded to ensure that our study only included sources in the 500 $\deg^2$ footprint.

To find the AGN specifically in the survey field, we took the SPT point source catalog and compared it to

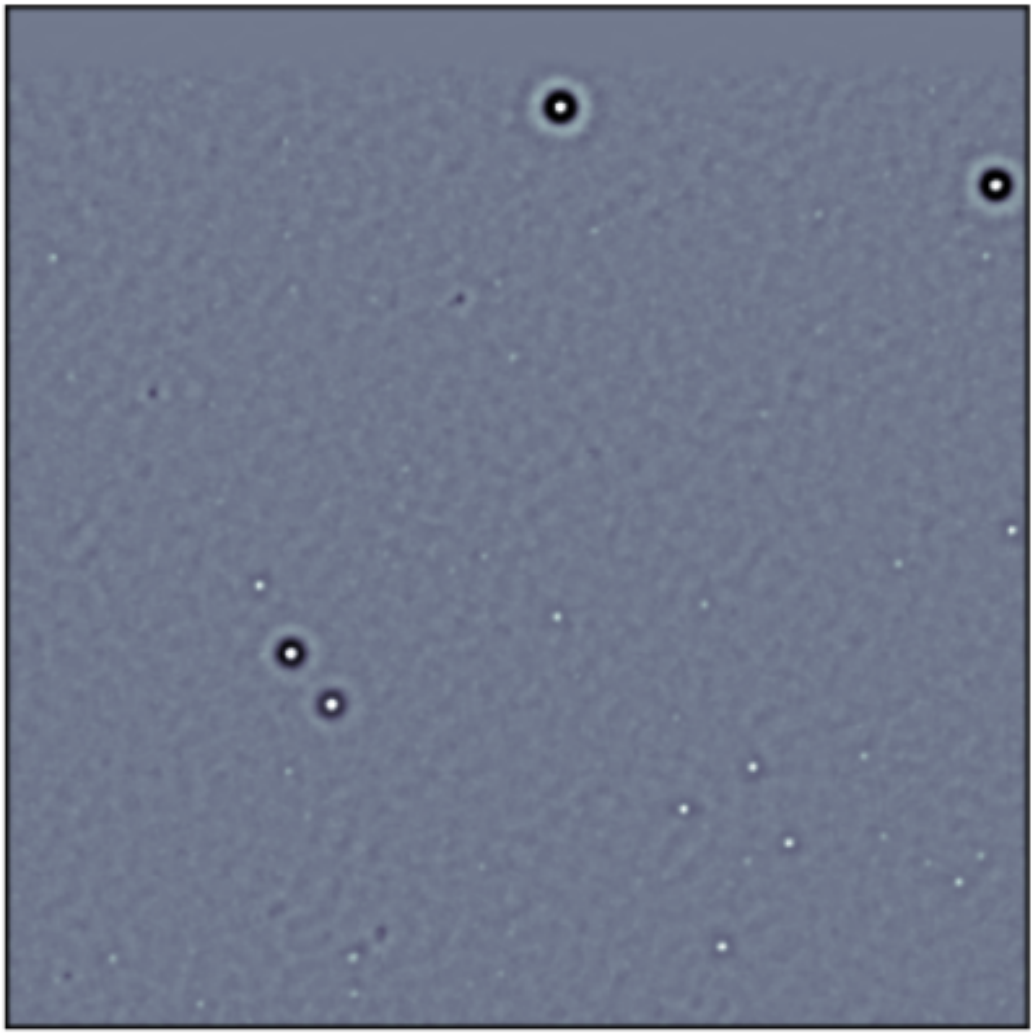

Figure 2.5: 5 x 5 degree section of matched filtered map.

the AT20G catalog. This allowed us to distinguish bright AGN from other bright objects such as dusty star forming galaxies. We used Fermi and SMARTS catalogs to determine if there were any cross matched observations of AGN in the field in those surveys. We marked these locations in our survey field; see Figure 2.8.

We found that there were $\sim$150 or so AGN in the field! Of those, two had observations in each of the surveys that have publicly available data. This discovery led to the pilot research study outlined in Chapter 3.

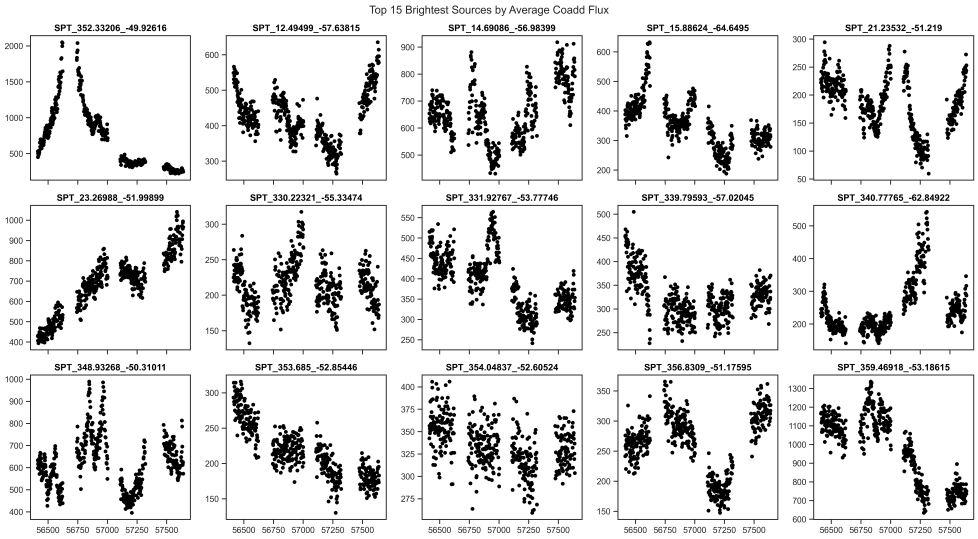

Figure 2.6: Light curves for the top 15 brightest AGN in the survey field.

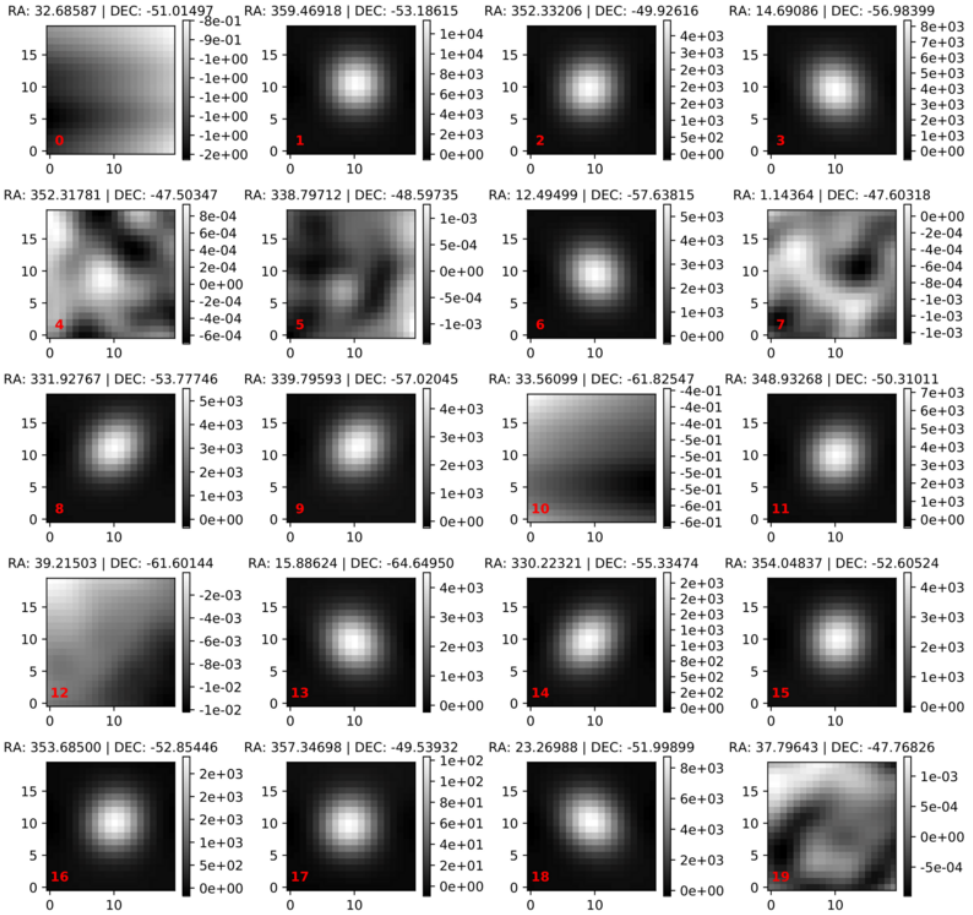

Figure 2.7: Snapshots of the filtered SPTpol map at locations of sources in the SPT-sz catalog. Sources within the SPTpol survey footprint appear as white spots, while locations outside of the SPTpol survey appear as noise.

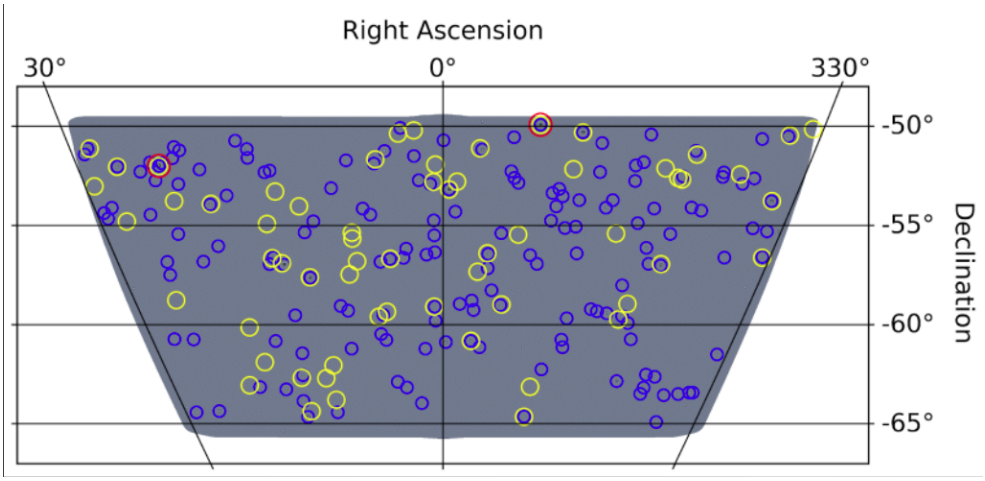

Figure 2.8: 500 deg^2 field with cross matched AGN marked. FERMI 4FGL(yellow), SMARTS(red), SPT $\times$ $AT20G(blue)$.

CHAPTER 3

SIMULTANEOUS MILLIMETER-WAVE, GAMMA-RAY, AND OPTICAL MONITORING OF THE BLAZAR PKS 2326-502 DURING A FLARING STATE

The following work will be submitted to the Astrophysical Journal Letters and is reprinted below in its entirety

Simultaneous Millimeter-wave, Gamma-ray, and Optical Monitoring of the Blazar PKS 2326-502 During a Flaring State

J. C. Hood[1,2,3,4], A. Simpson[5], P. A. R. Ade[7], M. Ajello[46]A. J. Anderson[8], E. AnderesJ. E. Austermann[9], J. S. Avva[10], J. A. Beall[9], A. N. Bender[2,11], B. A. Benson[2,3,8], F. Bianchini[6], L. E. Bleem[2,11], J. E. Carlstrom[2,3,11,12,13], C. L. Chang[2,3,11], P. Chaubal[6], H. C. Chiang, T-L. Chou[212]R. Citron[4], C. Corbett Moran[14], T. M. Crawford[2,3], A. T. Crites[2,3,15], T. de Haan[10,16], C. M. Daley[20]M. A. Dobbs[17,18], W. Everett[19], C. Feng[20,21], J. Gallicchio[2,22], E. M. George[10,23], N. Goeckner-Wald[26], S. Guns[10], N. Gupta[6], A. Gilbert[17], N. W. Halverson[19,24], N. Harrington[10], J. W. Henning[2,11], G. C. Hilton[9], G. P. Holder[18,20,21], W. L. Holzapfel[10], Z. Hou[2], J. D. Hrubes[4], N. Huang[10], J. Hubmayr[9], K. D. Irwin[25,26], L. Knox[27], A. T. Lee[10,16], D. Li[9,25], A. Lowitz[4], D. Luong-Van[4], D. P. Marrone[28], A. McDaniel[46]J. J. McMahon[2,3], S. S. Meyer[2,3,12,13], L. M. Mocanu[2,3], J. Montgomery[17], A. Nadolski[20,21], T. Natoli[12,2,33], J. P. Nibarger[9], G. I. Noble[17], V. Novosad[34], Y. Omori[2], S. Padin[2,3,15], S. Patil[6], C. Pryke[35], C. L. Reichardt[6], J. E. Ruhl[37], B. R. Saliwanchik, J.T. Sayre[19,24], K. K. Schaffer[2,13,38], E. Shirokoff[10,2,3], C. Sievers[4]G. Smecher[17,39], Z. Staniszewski[37,40], A. A. Stark[41], K. T. Story[26,42], E. R. Switzer[2,43], C. Tucker[7], K. Vanderlinde[33,44], T. Veach[45], J. D. Vieira[20,21], G. Wang[11], N. Whitehorn[36], R. Williamson[4,40], W. L. K. Wu[2], V. Yefremenko[11], and L. Zhang[20]

[1]Department of Physics and Astronomy, Vanderbilt University, Nashville, TN, 37235

[2]Kavli Institute for Cosmological Physics, University of Chicago, 5640 South Ellis Avenue, Chicago, IL, USA 60637

[3]Department of Astronomy and Astrophysics, University of Chicago, 5640 South Ellis Avenue, Chicago, IL, USA 60637

[4]University of Chicago, 5640 South Ellis Avenue, Chicago, IL, USA 60637

[5]Department of Physics, Rensselaer Polytechnic Institute, Troy, NY 12180 [6]School of Physics, University of Melbourne, Parkville, VIC 3010, Australia

[7]Cardiff University, Cardiff CF10 3XQ, United Kingdom
[8]Fermi National Accelerator Laboratory, MS209, P.O. Box 500, Batavia, IL 60510
[9]NIST Quantum Devices Group, 325 Broadway Mailcode 817.03, Boulder, CO, USA 80305
[10]Department of Physics, University of California, Berkeley, CA, USA 94720
[11]High Energy Physics Division, Argonne National Laboratory, 9700 S. Cass Avenue, Argonne, IL, USA 60439
[12]Department of Physics, University of Chicago, 5640 South Ellis Avenue, Chicago, IL, USA 60637
[13]Enrico Fermi Institute, University of Chicago, 5640 South Ellis Avenue, Chicago, IL, USA 60637
School of Mathematics, Statistics & Computer Science, University of KwaZulu-Natal, Durban, South Africa
[14]TAPIR, Walter Burke Institute for Theoretical Physics, California Institute of Technology, 1200 E California Blvd, Pasadena, CA, USA 91125
[15]California Institute of Technology, MS 249-17, 1216 E. California Blvd., Pasadena, CA, USA 91125
[16]Physics Division, Lawrence Berkeley National Laboratory, Berkeley, CA, USA 94720
[17]Department of Physics, McGill University, 3600 Rue University, Montreal, Quebec H3A 2T8, Canada
[18]Canadian Institute for Advanced Research, CIFAR Program in Cosmology and Gravity, Toronto, ON, M5G 1Z8, Canada
[19]Department of Astrophysical and Planetary Sciences, University of Colorado, Boulder, CO, USA 80309
[20]Astronomy Department, University of Illinois at Urbana-Champaign, 1002 W. Green Street, Urbana, IL, USA 61801
[21]Department of Physics, University of Illinois Urbana-Champaign, 1110 W. Green Street, Urbana, IL, USA 61801
[22]Harvey Mudd College, 301 Platt Blvd., Claremont, CA 91711
[23]European Southern Observatory, Karl-Schwarzschild-Str. 2, 85748 Garching bei München, Germany
[24]Department of Physics, University of Colorado, Boulder, CO, USA 80309
[25]SLAC National Accelerator Laboratory, 2575 Sand Hill Road, Menlo Park, CA 94025
[26]Dept. of Physics, Stanford University, 382 Via Pueblo Mall, Stanford, CA 94305
[27]Department of Physics, University of California, One Shields Avenue, Davis, CA, USA 95616
[28]Steward Observatory, University of Arizona, 933 North Cherry Avenue, Tucson, AZ 85721
[29]Department of Physics, University of Michigan, 450 Church Street, Ann Arbor, MI, USA 48109
[30]Faculty of Physics, Ludwig-Maximilians-Universität, Scheinerstr. 1, 81679 Munich, Germany
[31]Excellence Cluster Universe, Boltzmannstr. 2, 85748 Garching, Germany
[32]Max Planck Institute for Extraterrestrial Physics, Giessenbachstr. 85748 Garching, Germany
[33]Dunlap Institute for Astronomy & Astrophysics, University of Toronto, 50 St George St, Toronto, ON,

M5S 3H4, Canada

[34]Materials Sciences Division, Argonne National Laboratory, 9700 S. Cass Avenue, Argonne, IL, USA 60439

[35]School of Physics and Astronomy, University of Minnesota, 116 Church Street S.E. Minneapolis, MN, USA 55455

[36]Department of Physics and Astronomy, University of California, Los Angeles, CA, USA 90095

[37]Physics Department, Center for Education and Research in Cosmology and Astrophysics, Case Western Reserve University, Cleveland, OH, USA 44106

[38]Liberal Arts Department, School of the Art Institute of Chicago, 112 S Michigan Ave, Chicago, IL, USA 60603

[39]Three-Speed Logic, Inc., Vancouver, B.C., V6A 2J8, Canada

[40]Jet Propulsion Laboratory, California Institute of Technology, Pasadena, CA. USA 91109

[41]Harvard-Smithsonian Center for Astrophysics, 60 Garden Street, Cambridge, MA, USA 02138

[42]Kavli Institute for Particle Astrophysics and Cosmology, Stanford University, 452 Lomita Mall, Stanford, CA 94305

[43]NASA Goddard Space Flight Center, Greenbelt, MD 20771

[44]Department of Astronomy & Astrophysics, University of Toronto, 50 St George St, Toronto, ON, M5S 3H4, Canada

[45]Department of Astronomy, University of Maryland College Park, MD, USA 20742

3.1 Abstract

While continuous high-cadence monitoring of active galactic nuclei (AGN) is common at γ-ray, optical, and radio wavelengths, AGN monitoring in the millimeter (mm) band has mostly been restricted to short campaigns on targeted sources.Cosmic microwave background (CMB) experiments can now monitor these objects daily in increasingly large areas of sky. We present temporal monitoring of the active galactic nuclei PKS2326-502 from month/year to month/year with a temporal resolution of 36 hours. The flux of PKS 2326-502 is measured at high significance in each 36 hour period (typically S/N = 221.45 — 2052.45). We use SPT 150 GHz observations to create AGN light curves in the mm band and compare those to light curves at other wavelengths, in particular γ-ray and optical. our focus source is the blazar-type AGN PKS 2326-502, which has extensive, day-timescale monitoring at γ-ray, optical, and millimeter wavelengths between 2013 and 2016. We find PKS 2326-502 to be in a flaring state in the first two years of this monitoring, and we present a search for evidence of correlated variability between SPT (150 GHz), SMARTS (R band) and *Fermi* (γ-ray) observations. This pilot study paves the way for far larger AGN monitoring campaigns with current

and upcoming CMB experiments such as SPT-3G, Simons Observatory, and CMB-S4. These mm-wavelength AGN monitoring campaigns will enhance multi-wavelength studies with facilities such as VRO-LSST.

AGN — variability — SPT — SMARTS — Fermi — millimeter

3.2 Introduction

AGN are actively accreting supermassive ($10^5 < M_\odot < 10^9$) black holes that are commonly found at the centers of massive galaxies (Kormendy and Richstone, 1995; Gebhardt et al., 2000; Carroll and Ostlie, 2007). The Unified Model of AGN[1] proposes to explain observed categories of AGN via a scenario where the appearance of a source depends on the angle of the axis of symmetry of the source from our line of sight(Antonucci, 1993; Urry and Padovani, 1995). The spectral energy distribution (SED) of blazars has a characteristic double-humped structure, with one peak located anywhere from the high-frequency radio to the soft X-ray band, caused by synchrotron emission from energetic electrons in the blazar jet, and a high-energy peak in the MeV-TeV γ-ray band, with the location of such peaks dependent on the luminosity of the source (Fossati et al., 1998). Attempts to explain this double-humped structure can be classified into two classes of models that invoke three different physical mechanisms (e.g., Blandford et al., 2019). These models are the hadronic and leptonic models: In the hadronic model, processes such as photo-pion production are responsible for the γ-ray-ray peak, while in the leptonic models, the γ-ray peak is caused by inverse-Compton scattering of lower-energy photons. These lower-energy photons can be the same synchrotron photons responsible for the low-energy peak (the "synchrotron self-Compton" model) or other components of the radiation field such as the radiation from the accretion disk, or the Broad Emission Region (the "external inverse-Compton" model, Sikora et al. 1994).

A key to distinguishing between these models is what they predict for multi-wavelength observations of blazar flares. Leptonic models have been very successful in explaining several observed aspects of blazars (Sikora et al., 1994; Sikora and Madejski, 2003). The simplest interpretation of leptonic models predict that when observing AGN light curves in multiple wavelengths, there should be correlated variability between the synchrotron peak (optical/infrared observations) and the high energy peak (γ-ray observations). This behavior has been observed in many cases (see, e.g., Bonning et al. 2009), but previous studies provide evidence that this may not always be true. For example, in the multi-wavelength study of PKS 0208-502, there was an observed anomalous outburst or "orphan flare," in which a significant flux increase is seen in the optical/IR bands but not in the γ-ray band (Chatterjee et al., 2013a,b).

Both radio and mm-wave radiations are strong tracers of synchrotron emission. As such, observations of those spectral regimes should serve as another promising piece of the puzzle to help identify the true origin of

[1] Radio-loud AGN are generally defined as AGN with a ratio of radio (5 GHz) to optical (B-band) flux ≥ 10 (Kellermann et al., 1989).

the blazar SED, and in particular, the source of radiating particles. Multi-wavelength studies of blazar flares have traditionally included γ-ray, X-ray, optical, infrared, and radio emission. Since mm-wave radiation is a strong tracer of synchrotron emission, observations in this regime of AGN should serve as another promising piece of this puzzle to help identify the true origin of the blazar SED. Recent studies show that on longer timescales, mm-wave variability is better correlated with γ-ray emission than optical (Meyer et al., 2020), while on shorter timescales features tend to correlate more between the optical and γ-ray. This points toward the possibility of synchrotron emission produced in different regions of the blazar being responsible for the mm–γ-ray correlations and the optical–γ-ray correlations.

While mm emission has been included in AGN variability studies of a handful of targeted sources (e.g., Meyer et al., 2020), the field currently lacks systematic monitoring in the mm over large patches of sky. We are in the process of remedying this situation by taking advantage of cosmic microwave background (CMB) experiments as AGN monitors. AGN appear as bright point sources in maps made by CMB experiments, and current CMB experiments are sufficiently sensitive to detect many AGN at high S/N ($>$10) in short (less than 1 day) observations. When combined with an observing strategy that results in high-cadence observations of the same patch of sky over many years, CMB data-sets are very effective for AGN monitoring. We have made an initial study into mm-wave AGN variability using data taken with the South Pole Telescope (SPT) second-generation camera SPTpol. The SPTpol survey enables the monitoring of tens of mm-bright AGN on timescales from years to days at high S/N ($>$ 10 in a 36-hour coadd). These observations provide the opportunity to include mm-wave AGN monitoring in the study of the physical mechanisms behind AGN emission.

Although our SPTpol AGN monitoring campaign includes tens of sources, we choose to focus on the blazar PKS 2326-502 for this pilot study because of its long history of observations in multiple wavelengths (Dutka et al., 2017). PKS 2326-502 is a flat-spectrum radio quasar (FSRQ) at redshift $z = 0.518$ and is among the targets of monitoring by both the Fermi-LAT and Yale-SMARTS Blazar Group collaborations. Thus PKS 2326-502 has a wealth of publicly available (*Fermi*) γ-ray, (SMARTS) optical R band, and infrared observations to compare to our mm-wave (150 GHz SPTpol) observations.

3.3 Observations

To study the correlated variability in multi-wavelength light curves of PKS 2326-502, we use data from *Fermi*-LAT, SMARTS and SPT (150 GHz). In this section, we describe the observations and data reduction for each instrument.

3.3.1 SPT

The SPT (Carlstrom et al., 2011) is a 10-meter telescope located at the geographic South Pole and dedicated to making low-noise, high-resolution maps of the mm-wave sky, with the primary goal of mapping the temperature and polarization anisotropies in the CMB. Three separate cameras have been installed on the telescope, each used to map multiple large patches of the Southern Celestial Hemisphere. This work involves a pilot study using data from the second-generation camera, SPTpol. From 2013 - 2016 SPTpol was used to survey 500 $\deg^2$ of the southern extragalactic sky at arc minute resolution to milli-Jansky levels. The 500 $\deg^2$ SPTpol survey consists of $\sim$3500 observations over $\sim$9000 hours at high Galactic latitude, covering 22^h to 2^h in right ascension and -65° to -50° in declination (Henning et al., 2018). For studies of the CMB, these observations were combined into a four-year coadd map. However, for this study we take the individual observations and combine them into 36 hour bundles. The 36 hour bundle time was chosen due to is being the length of the instruments cryogenic observing day. Once these bundle maps are created, we apply a matched filter that removes the long wavelength modes from each map, maximizing the S/N on point sources. These filtered bundles have a 1σ error of $\sim$5 mJy providing us with S/N $>$10 in a 36 hour bundle on 25 AGN in the 500 $\deg^2$ field. We then extract the flux for all of the bright sources in the SPT catalog that are associated with a source in the AT20G catalog (Murphy et al., 2010b). This cross-matching is done to differentiate the AGN from other point sources like dusty star forming galaxies found in the SPT source catalog. Once the cross matching has been confirmed, a series of calibration corrections were conducted. An astrometry check verified that the sources were properly located in the maps, while a calibration check corrected the absolute calibration of each map by comparing it to a full-depth map from the Planck satellite. We additionally checked for contamination from the sun which would appear as bright streaks in our observations by plotting 20 x 20 pixel patches of sky centered on PKS2326-502 to check for any additional maps that needed to be removed. Once all maps have been calibrated and checked, we extract the millimeter fluxes that are used to create the mm-wave light curve described in this pilot study.

3.3.2 SMARTS

This paper makes use of up-to-date Small and Moderate Aperture Research Telescope System (SMARTS) optical/near-infrared light curves that are available at the SMARTS website.[2] The SMARTS telescope is located in Cerro Tololo Chile, and thus very well suited to monitoring of Southern Hemisphere targets. The SMARTS blazar sample was initially (in 2008) defined to include all *Fermi*-LAT-monitored blazars on the initial public release list with declination $< 20°$. Observations were made in the B, V, R, J & K bands, with an observing cadence of 1 - 3 days. Here, we use the 1 day cadence optical R band observations to match

[2] www.astro.yale.edu/smarts/glast/home.php

the SPT cadence as closely as possible. The full details of the data selection and analysis procedure for Yale-SMARTS, can be found in Bonning et al. (2012).

3.3.3 Fermi LAT

The *Fermi*-LAT light curve for PKS 2326-502 is taken from the *Fermi*-LAT Light Curve Repository (LCR, Fermi Large Area Telescope Collaboration 2021).[3] The LCR is a public database of multi-cadence flux calibrated light curves for over 1500 variable sources in the 10-year *Fermi*-LAT point source catalog (4FGL-DR2, Ballet et al. 2020). The light curves generated by the LCR span the duration of the mission and are obtained by performing an unbinned likelihood analysis over the energy range between 100 MeV–100 GeV. The LCR analysis uses the standard *Fermi*-LAT Science Tools (version v11r5p3) and the P8R2_SOURCE_V6 instrument response functions on P8R3_SOURCE class photons. Photons are selected from a 12° region of interest (ROI) centered on the location of the 4FGL-DR2 counterpart of PKS 2326-502 (4FGL J2329.3-4955). A zenith angle cut of 90° is used to prevent contamination from the Earth's limb. Included in the model are all 4FGL-DR2 point sources within 30° as well as galactic diffuse (gll_iem_v07.fits) and isotropic (iso_P8R3_SOURCE_V3_v1) background models. The LCR provides light curves in cadences of 3 days, 1 week, and 1 month. For this analysis we use the minimum available time binning of 3 days.

3.4 Methods

Here we report both qualitative and quantitative results from the analysis of multi-wavelength light curves (mm, optical and γ-ray). We focus on the observations made in the first two years of available SPTpol data (2013-2014), because: 1) PKS 2326-502 entered into a quiescent state thereafter, and 2) there is no publicly available optical data from SMARTS after 2014. Quantitatively, we measure the local cross correlation functions (CCFs) of year-long light curves and calculate the significance by comparing these to uncorrelated simulations. The simulations used here were created by taking the power spectrum of the light curve from each data set, fitting to a model in which $P(f) = P_0(1 + (f/f_{\rm knee})^{-\alpha})$, and producing 10,000 simulations of light curves from each model power spectrum. The simulated light curves are generated in Fourier space with random phase (i.e., they obey Gaussian statistics in real space). Some recent results have indicated that, at least in the γ-ray, blazar variability is better described by a log-normal probability distribution than a Gaussian (e.g., Duda and Bhatta, 2021). We have created an alternate set of simulations with log-normal statistics and do not see any significant change in our results when we use this alternate set.

We calculate the local CCF for each pair of light curves in the real data and all 10,000 simulations using the following procedure. For a given time lag bin τ, we select all data points in light curves a and b that

[3] https://fermi.gsfc.nasa.gov/ssc/data/access/lat/LightCurveRepository/

satisfy:

$$t(a) - t(b) \in \tau \pm \Delta\tau, \tag{3.1}$$

where $\Delta\tau$ is the bin width, and $t(a)$ and $t(b)$ are the times for observations in each light curve. We define the local CCF as:

$$CCF(\tau) = \frac{\sum_{i=1}^{n}(a_i - \bar{a})(b_i - \bar{b})}{(n-1)s_a s_b}, \tag{3.2}$$

where s_a is defined as:

$$s_a = \sqrt{\frac{1}{n-1}\sum_{i=1}^{n}(a_i - \bar{a})^2}, \tag{3.3}$$

$\bar{a}$ is defined as:

$$\bar{a} = \frac{1}{n}\sum_{i=1}^{n} a_i \tag{3.4}$$

and i runs over all pairs of points that satisfy Equation 3.1. The simulated CCFs were then used to find the 1σ, 2σ and 3σ envelopes for the local CCF.

As discussed in Welsh (1999), the full correlation function and any attempt to determine a lag are challenging in data that is dominated by the longest time-scale feature in the data. For this reason, we only calculate the zero-lag correlation and associated p-value for unfiltered data. This p-value is estimated by calculating the number of simulations that have a higher zero-lag correlation than the data:

$$P(CCF, \tau = 0) = \frac{N(CCF_{\rm sim}, \tau = 0 > CCF_{\rm data}, \tau = 0)}{N_{\rm sims}} \tag{3.5}$$

To investigate the full correlation function and to highlight shorter-timescale features we polynomially filtered the data. We applied a fifth order polynomial filter, which preserves features on $\sim 0-6$ month-long time scales. We also report the zero-lag correlation and zero-lag p-value of data that has been smoothed by a boxcar average with a window of 7 days. This smoothing removes any possible dependencies on the binning from our reported p-values.

3.5 Results

Multi-wavelength (γ-ray, optical, mm) light curves for the four years of monitoring of PKS 2326-502 are shown in Figure 3.1. We note that the raw statistical significance of the variability in all three bands is very high: The typical signal-to-noise ratio (SNR) in the SPT light curve is $\sim$50 in the quiescent state and over 200 in the flaring state, and corresponding values for the *Fermi* light curve are 1–2 and 7–10. For SMARTS-R, where we only have data in the flaring state, the typical SNR is $\sim$50.

Several features of these light curves which make up the primary results of this letter are evident by-eye in Figure 3.1, including:

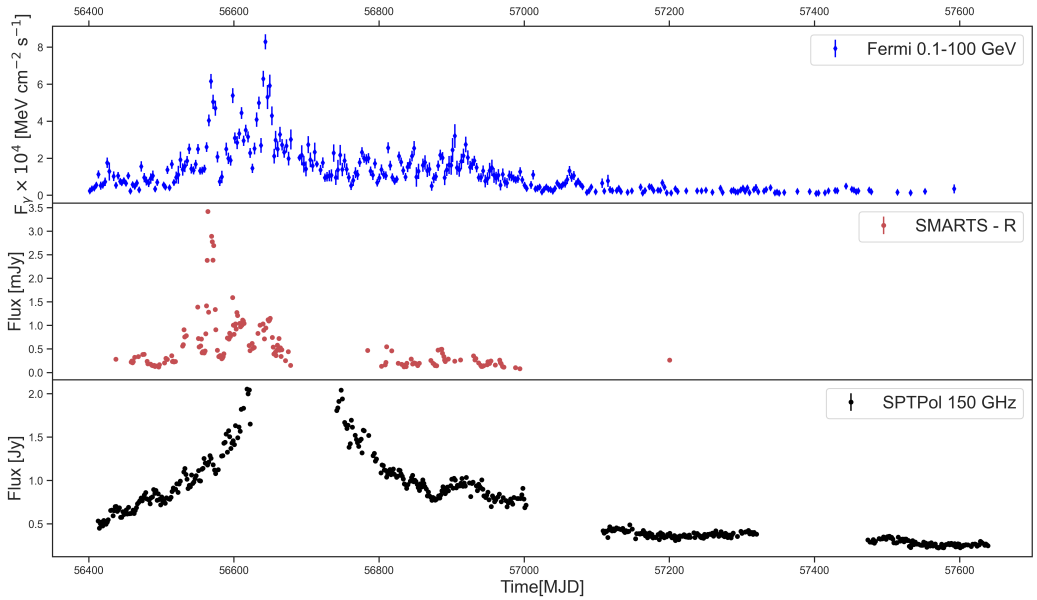

Figure 3.1: Light curves for FSRQ PKS 2326-502. top: Fermi-LAT; middle: SMARTS optical R; bottom: SPT 150GHz. here we can see long-timescale correlation between mm and γ-ray observations and short-timescale correlations between the optical and γ-ray observations.

1. Long-timescale flaring state in the first 2 years followed by a 2 year quiescent period.
2. Long-timescale correlations between mm and γ-rays.
3. Short-timescale correlations between γ-ray and optical data.

As discussed in Section 3.4, we use several tools in an attempt to assess these features quantitatively. As a rough measure of the significance of the correlated year time-scale flare in γ-ray and mm, we calculate the number of simulations that show a similar or larger flux increase over one year in those two bands. We find that only 42 out of 10,000 simulations show a factor of 2.5 increase over one year in both bands. We chose a factor of 2.5 because the ratio of the last month's vs. first month's flux was 2.7 in SPT and 3.3 in *Fermi*. Therefore, we report 0.0042 as a raw, non-trials-corrected p-value for this long-timescale correlated flaring state. We also calculate the zero-lag correlation for the unfiltered year one data and we find a zero-lag correlation value of 0.6934 for SPT x *Fermi*. Only 259 simulations show a zero-lag correlation between SPT x *Fermi* higher than this, thus we report in Table 3.1 a p-value of 0.0259 for this correlation.

Another fairly strong identifiable feature in the data is the short $\sim$week-long-timescale flare seen in both *Fermi* and SMARTS but not in SPT. This leads to a fairly significant detection of zero-lag correlation even in the unfiltered data $P(CCF, \tau = 0) = 0.001$. Once we filter out the long time-scale features we find a zero-lag correlation value much higher than found in any of our simulations and thus report a p-value of $< 10^{-4}$ in Table 3.1. This confirms that this correlation is being driven by the shorter-timescale feature in the *Fermi* and

SMARTS light curves shown in Figure 3.2. By contrast, when we filter SPT x *Fermi* data in year one, we find no evidence of correlations on shorter timescales in year one, while in the year two de-trended data, we show a significant zero-lag detection of $P(CCF, \tau = 0) = 0.0054$.

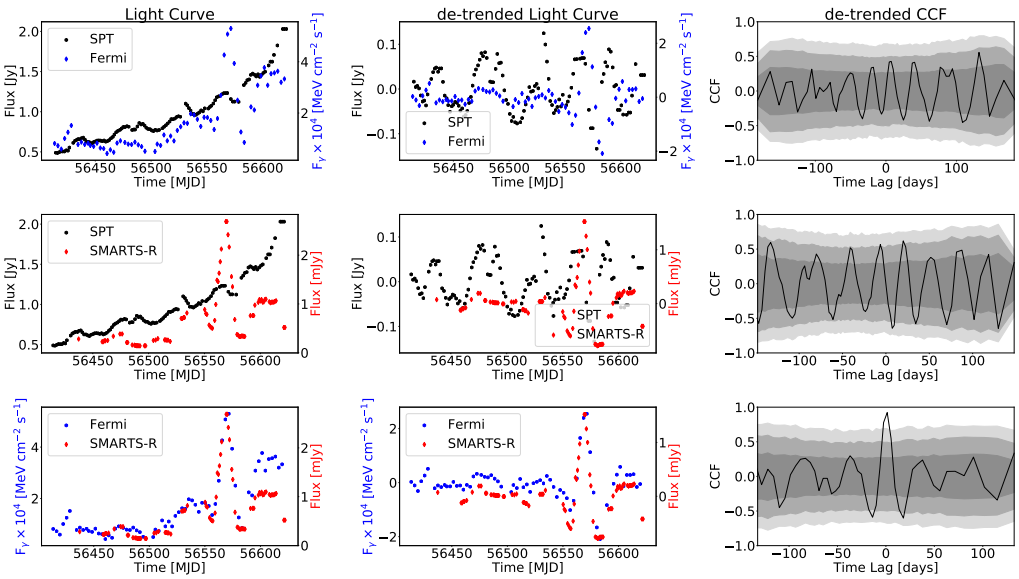

Figure 3.2: Year one boxcar smoothed light curves (left column), year one boxcar smoothed and de-trended light curves (middle column), year one detrended light curve cross correlation functions (right column). The grey shaded regions represent the 1σ, 2σ and 3σ envelopes of simulated CCFs.

For year two, we report a significant correlation between the filtered and de-trended SPT x *Fermi*light curves, but none for the SMARTs X *Fermi*data as seen in the previous year. (Year two light curves and de-trended CCF's are shown in Figure 3.3.) Similarly we find no significant correlations between the unfiltered or de-trended SPT and SMARTS data in either year's observations. Finally we note that we measure no significant correlations at non-zero lag for any data combination.

3.6 Discussion

Our study of the multi-wavelength variability of PKS 2326-502 yields three basic results:

1. Clear long-timescale correlations between γ-ray and mm-wave light curves.
2. Clear short-timescale correlations between γ-ray and optical light curves.
3. No measurable correlation between mm-wave and optical light curves.

These results have implications for the production mechanism of γ-rays in blazars and the structure of these systems in general, possibly adding motivation to revisit the Unified model. The strong correlations on short time scales seen in year one but not year two for the Fermi x SMARTS light curves do agree with

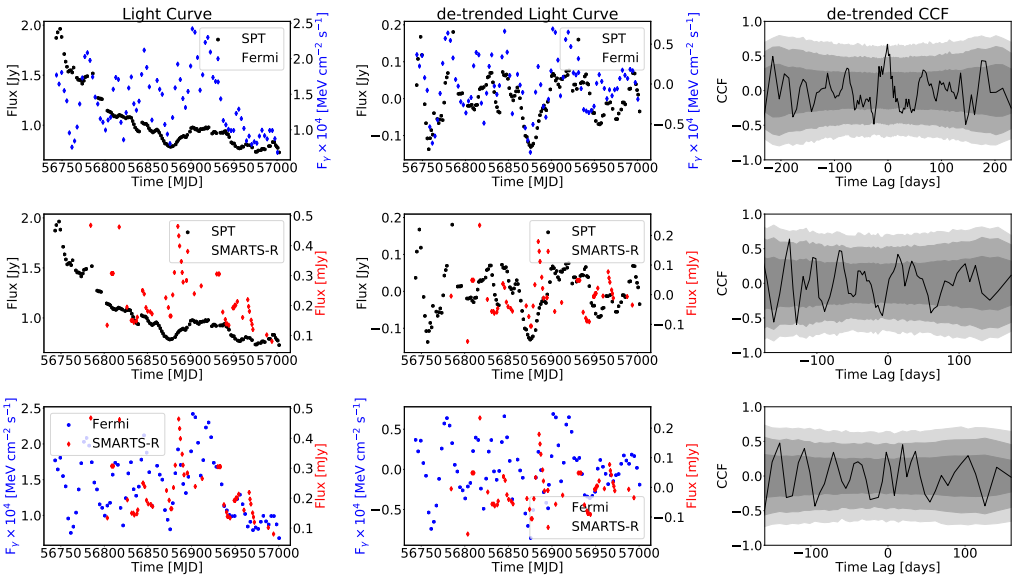

Figure 3.3: Year two boxcar smoothed light curves (left column), year two boxcar smoothed and de-trended light curves (middle column), year two detrended light curve cross correlation functions (right column). The grey shaded regions represent the 1σ, 2σ and 3σ envelopes of simulated CCFs.

Light Curve Statistics		
Dataset	zero-lag correlation	zero-lag p-value
SPT x Fermi year one (raw)	0.6934	0.0259
SPT x Fermi year one (de-trended)	0.0745	0.3519
SPT x Fermi year one (smoothed)	-0.0488	0.5688
Smarts x Fermi year one (raw)	0.8012	0.0010
Smarts x Fermi year one (de-trended)	0.7249	$< 10^{-4}$
Smarts x Fermi year one (smoothed)	0.9223	$< 10^{-4}$
SPT x Smarts year one (raw)	0.3994	0.1770
SPT x Smarts year one (de-trended)	0.0106	0.4880
SPT x Smarts year one (smoothed)	-0.0479	0.5657
SPT x Fermi year two (raw)	0.2632	0.2646
SPT x Fermi year two (de-trended)	0.4625	0.0054
SPT x Fermi year two (smoothed)	0.6698	0.0009
Smarts x Fermi year two (raw)	0.3766	0.1163
Smarts x Fermi year two (de-trended)	0.2432	0.1011
Smarts x Fermi year two (smoothed)	0.3444	0.0874
SPT x Smarts year two (raw)	0.2664	0.2738
SPT x Smarts year two (de-trended)	0.0378	0.4353
SPT x Smarts year two (smoothed)	0.0605	0.4135

Table 3.1: Values of zero-lag correlation and associated p-value for de-trended and unfiltered data, and values of the χ^2-like statistic, number of degrees of freedom, and associated p-value for the full CCF of de-trended data. Values for years one and two are reported separately.

traditional models for flaring behaviors. Additionally the lack of correlation between the SPT x SMARTS light curves, implies that the mechanisms that produce the two respective groups of synchrotron photons may be different. Furthermore, the high significance of the short time scale correlations for SPT x Fermi in year

two leads to further questions about the mechanisms behind AGN emissions.

3.7 Conclusion

We have presented results from a pilot study using multi wavelength light curves (γ-ray, mm, optical) of PKS 2326-502, in an attempt to gain new insight into the mystery of AGN γ-ray emission. While we found long-timescale correlations between the mm and γ-ray and short-timescale correlations between the optical and γ-ray, we found no correlations between the mm and optical. These results are broadly consistent with the leptonic Self Synchrotron Compton model of γ-ray production, but they imply that the production of synchrotron emission is more complex than a single source at all wavelengths.

While this study only used data from a single object, we have mm-wavelength data from many more AGN in the SPTpol survey that we are now looking to use to investigate these multi-wavelength correlations. We look to expand this monitoring program by exploiting the yet more sensitive data from the current camera on the SPT, SPT-3G (Sobrin et al., 2022). The bulk of SPT-3G time is being used to observe a 1500 deg^2 survey field. Thus, SPT-3G will not only increase the number of possible sources to include in further studies but will also provide AGN light curves with increased sensitivity. In addition to expanding this AGN monitoring into the SPT-3G survey, we also look to use the data from future experiments to expand our AGN monitoring program. The CMB-S4 (Abazajian et al., 2016a) and Simons Observatory (Ade et al., 2019) experiments combined with current mm-wave observatories will cover up to 70% of the sky at nearly daily cadences. With the mm-wave sky having a larger footprint, it will pair well with future optical survey observatories such as VRO-LSST (Ivezić et al., 2019) for multi-wavelength AGN studies. CMB experiments are poised to become an integral part of the AGN monitoring landscape.

CHAPTER 4

MICROWAVE DETECTOR DEVELOPMENT AND TESTING: ROOM TEMPERATURE MEASUREMENTS

f

4.1 Introduction

This section will describe in detail the initial testing of new detectors for the CMB-S4 experiment. With new CMB experiments on the horizon, the development of detector technologies with increased sensitivity has been identified as a major focus point. One of these experiments, CMB-S4 or CMB "Stage-4," is the next generation ground based cosmic microwave background experiment. The CMB-S4 experiment (Abazajian et al., 2016b) seeks to explore the physics of inflation, dark matter, neutrinos, and dark energy through precision measurements of the anisotropies of the Cosmic Microwave Background radiation. A key objective for CMB-S4 is to search for the primordial B-mode signal predicted by inflation. Figure 4.1 shows current measurements of the CMB B-mode power spectrum from gravitational lensing. Going beyond these measurements requires more telescopes and many more detectors compared to previous or current experiments (500,000 detectors for CMB-S4 vs $\sim$10,000 currently, Abitbol et al. 2017b).

4.1.1 Detector Technologies

CMB-S4 is developing feedhorn-coupled Transition Edge Sensor (TES) bolometer arrays, similar to work described in McMahon (2004) and fielded on SPTpol (Austermann et al., 2012), ACTPol (Grace et al., 2014) and Advanced ACT (Henderson et al., 2016). In this detector architecture, the signal from the telescope is transmitted into a feedhorn where it is transduced on to the detector wafer via an Orthomode Transducer (OMT, see Figure 4.2). The OMT also separates the signal into two orthogonal polarizations. On the wafer, the signal is transmitted via a superconducting microstrip where it is filtered and eventually thermalized. The thermal signal is measured by a Transition Edge Sensor (TES) bolometer (Irwin and Hilton, 2005).

TES bolometers can be fully characterized through two kinds of tests: dark tests, which measure the intrinsic noise of the detectors (from phonon fluctuations), and optical tests, which measure the detector optical performance, including coupling efficiency and systematics. Our goal was to carry out both dark and optical tests to characterize the performance of these new detectors. Based on what we found, we will change the design and construction of the detector to improve its performance and the reliability of its production.

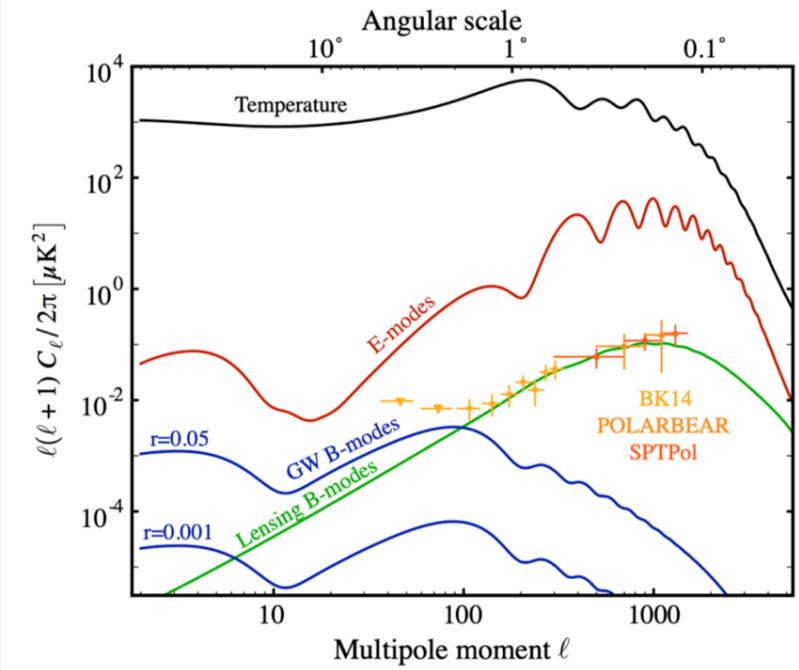

Figure 4.1: Theoretical predictions for the temperature (black), E-mode (red), B-mode (blue) power spectra. B-mode spectra are shown for two representative values r = 0.001 and r = 0.05. Also shown are expected values for the contribution to B modes from gravitationally lensed E modes (green). Current measurements of the B-mode spectrum are shown for the BICEP2/Keck Array (light orange marker), POLARBEAR (orange marker), and SPTPol (dark orange marker) from left to right respectively. Detecting the GW B-mode signal will require many more detectors relative to these experiments. Figure reproduced from: Abazajian et al. (2016b).

4.1.2 Transition Edge Sensor Bolometers

Large detector arrays for several applications, including CMB measurements, have been enabled by Transition Edge Sensor (TES) bolometers. These arrays are currently used by the SPT and Atacama Cosmology Telescope (ACT), enabling both intensity and polarization measurements. Figure 4.3 shows a cartoon of a bolometer and a plot of the superconducting-normal transition curve for a TES detector. TES measurements are made by large resistance changes in the sensor, caused by small temperature fluctuations in the absorber while it is in transition. The transition being talked about is the change between the normal state and the superconducting state of the metal, which is often niobium.

The shape and width of the transition region can be changed by adjusting the detector geometry and adding additional features to the superconducting structures connected to the TES (Chang et al., 2015). This transition is maintained by applying a constant or (bias) voltage across the TES. This bias voltage creates a strong negative electro-thermal feedback loop that allows the TES to self adjust its location within the superconducting transition region across a wide range of temperature fluctuations.

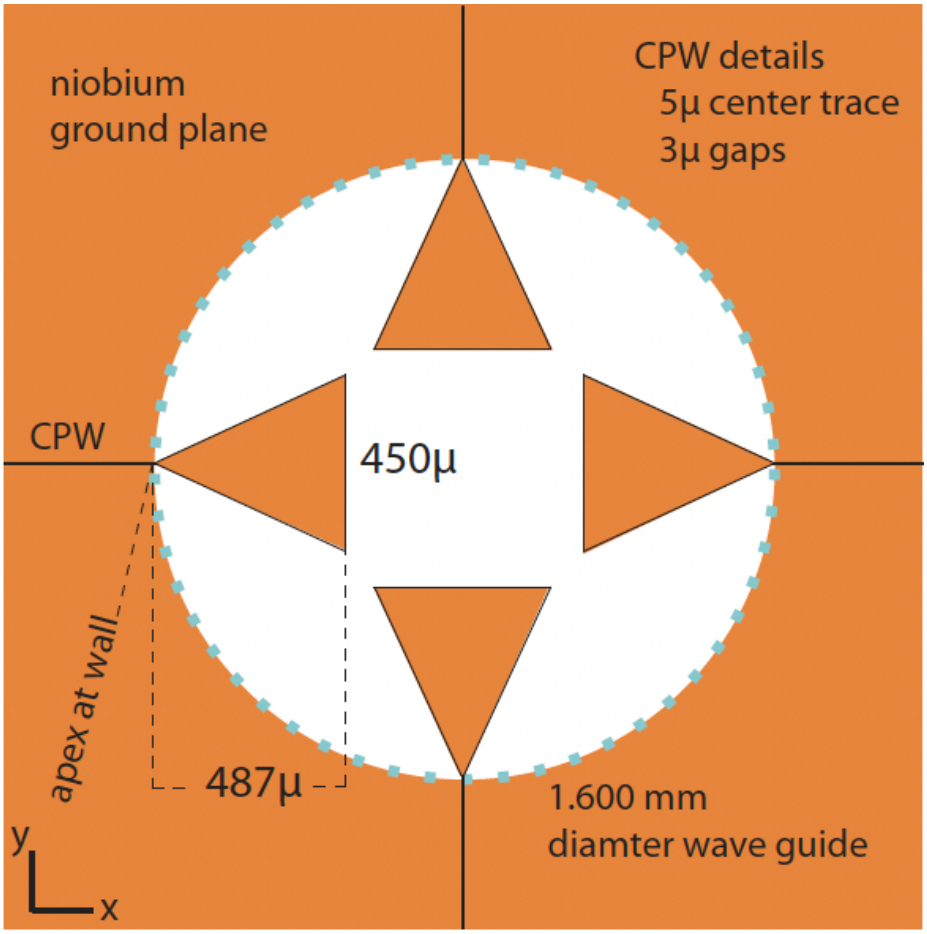

Figure 4.2: Example OMT window structure with each component labeled. Figure reproduced from McMahon et al. (2009).

4.2 Room Temperature Measurements

OMT coupled feed horn detectors are a candidate technology for CMB-S4. At Argonne National Laboratory, where all of the detector work we describe took place, we began developing fabrication processes for these types of antennas. In this chapter, we present a design for a room temperature experiment to measure the coupling properties of Argonne fabricated OMT's at 90 GHz. These warm measurements are conducted by coupling the test antenna to the OMT centered above a circular waveguide and choke structure. The test signal is injected down the circular waveguide where it couples to the OMT antennae. The signal on the antennae is then read out via a Vector Network Analyzer (VNA). The aim here was to use a simple room temperature setup to measure the polarization and coupling efficiency of candidate OMT structures. These room temperature measurements were conducted by first designing an OMT that was made of gold, since gold is conductive at room temperatures. We used these gold OMT structures to measure the loss across different lengths of microstrips that would have connected. In the sections that follow, we'll talk in detail

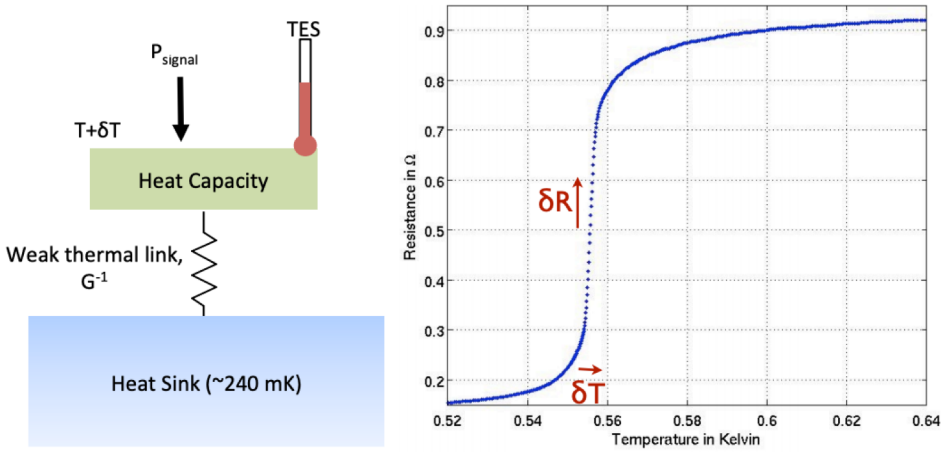

Figure 4.3: Left: Cartoon depiction of a bolometer. Incoming light hits an absorber, heating up a thermometer with heat capacity C. The thermometer is connected to a cold bath through a weak thermal link G. Right: Plot of resistance vs. temperature showing the superconducting transition of a TES. When operated at a point centered within the dotted region of the curve, the TES serves as a very sensitive thermometer. Figure reproduced from Abitbol et al. (2017a).

about how the experiment was set up and what the measurements at room temperature showed.

4.2.1 Experimental setup

In order to complete the necessary room temperature measurements, we needed to design a test chip that could be easily fabricated and geometrically altered. A plus-sign shaped test structure was selected since the OMT design would fit well and multiple signals could be probed. Figure 4.4 shows both the Solid Works model of a ∼550 micron thick outline of the shape of the test chip as well as the graphic model of the chip that was created using Graphics Data System via Python to create a mask that shows where the microstrip, OMT antennae, and other features are found. The fabrication of this chip would take this outline and mask the locations where gold was to be layered on the wafer.

The OMT window is created by a layer of Silicon Nitride that is between the silicon wafer and gold, as seen in Figure 4.6. The shape of the wafer is cut out of a larger wafer, and the OMT window is also removed using a chemical etching process.

With the chip design chosen, a mounting structure needed to be designed to hold the chip in place during testing. This structure needed a number of important components that would make taking the measurements as repeatable as possible. These requirements are listed here:

1. OMT back short depth machined to 1/4 measured wavelength.

2. Sufficient spacing between the chip and OMT window to allow slack.

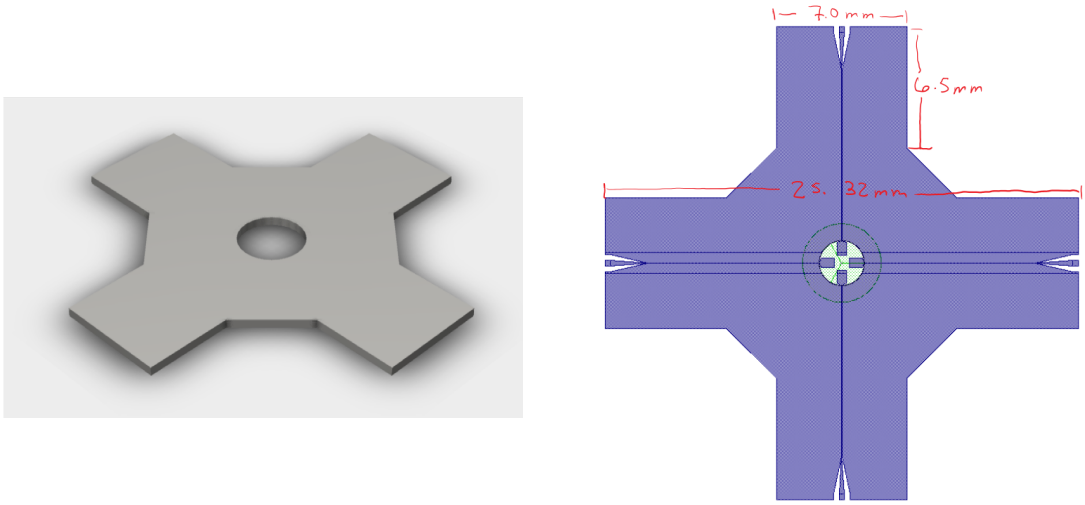

Figure 4.4: **Left:** Solidworks drawing of the shape the silicon wafer containing the test antenna. **Right:** GDS model of silicon wafer with dimensions.

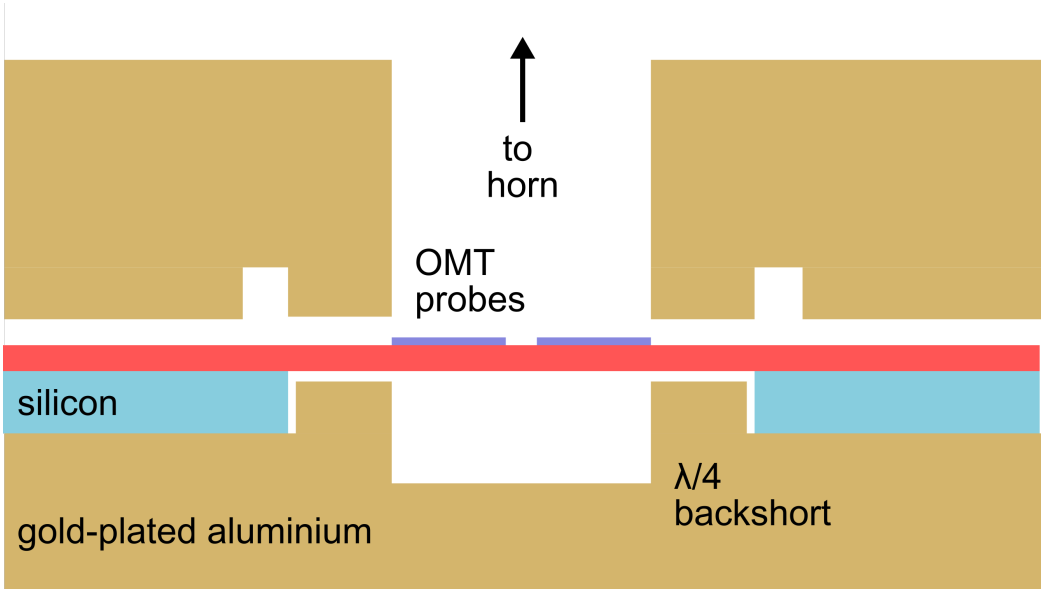

Figure 4.5: Visual of how the wafer fits into the base of the test block, focusing on the center OMT window.

3. Alignment pins to secure the chip.
4. Alignment pins between lid and base.
5. Mounting spaces for Edge Launch Connectors (ELCs).
6. Waveguide centered in lid above OMT window.

As seen in Figure 4.6, the base of the assembly is centered around the 220 GHz OMT backshort. Around the edges are the ledges where the test chip is elevated just above the window and held in place by the Edge

Launch Connectors (ELC's). The lid would then be attached to the base through alignment pins and screwed tight.

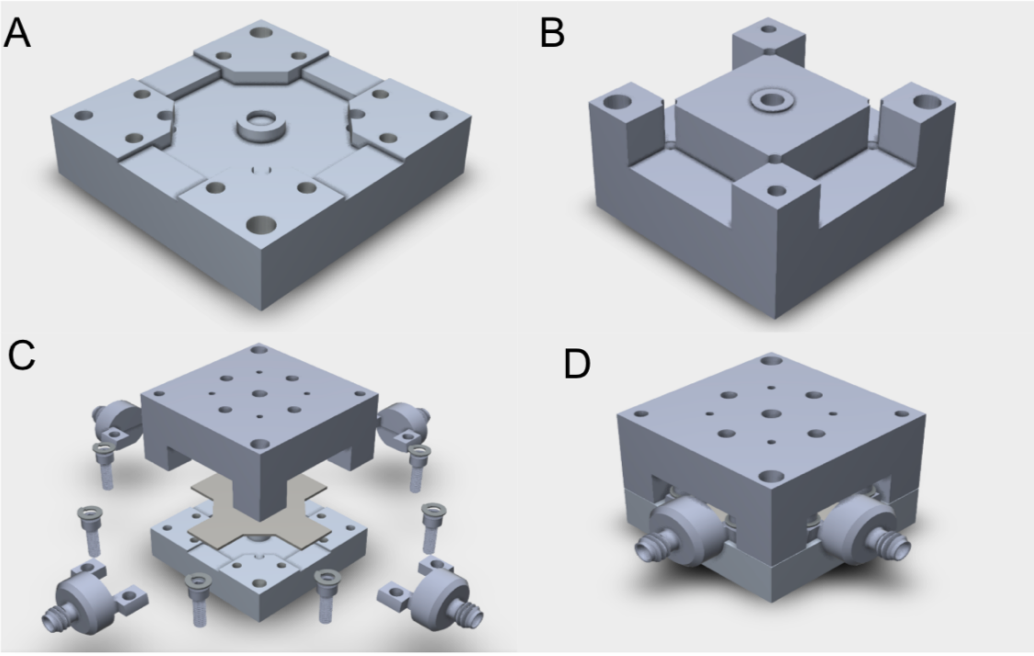

Figure 4.6: Solidworks models for: A) base of bracket and chip holder, B) lid of bracket, C) exploded view of entire assembly, D) complete assembly.

The device measurements were made by using a Vector Network Analyzer (VNA) to send a signal through the waveguide in the lid of the sample box and down onto the OMT antennae. The antennae would then absorb the signal and transmit it through the microstrip and down to the ELC's. The results of these measurements will be discussed in section 4.2.2.

In order to make our measurements, we identified all possible points of signal leakage and feedback-/reflection and took precautions to minimize their effects. As for any internal reflections, we put 50 Ohm terminating resistors on each microstrip lead that wasn't connected to the VNA's read-out line, as shown in Figure 4.7. This outline shows the path that the microwave signal produced by the VNA will follow once absorbed by the OMT probes. In this case, we are looking to measure the signal absorbed that travels down only one of the paths, representing roughly half of the total signal in that mode. The reason for the 50 Ohm resistors is to completely dampen out any possible reflections that may return from the ELC's.

4.2.2 Experimental Results

After making multiple measurements through our gold OMT test structures, we came to the conclusion that the gold was too resistant. While we were able to confirm that the design and geometry of the OMT probes were optically efficient, we were unable to make any significant signal measurements through our VNA

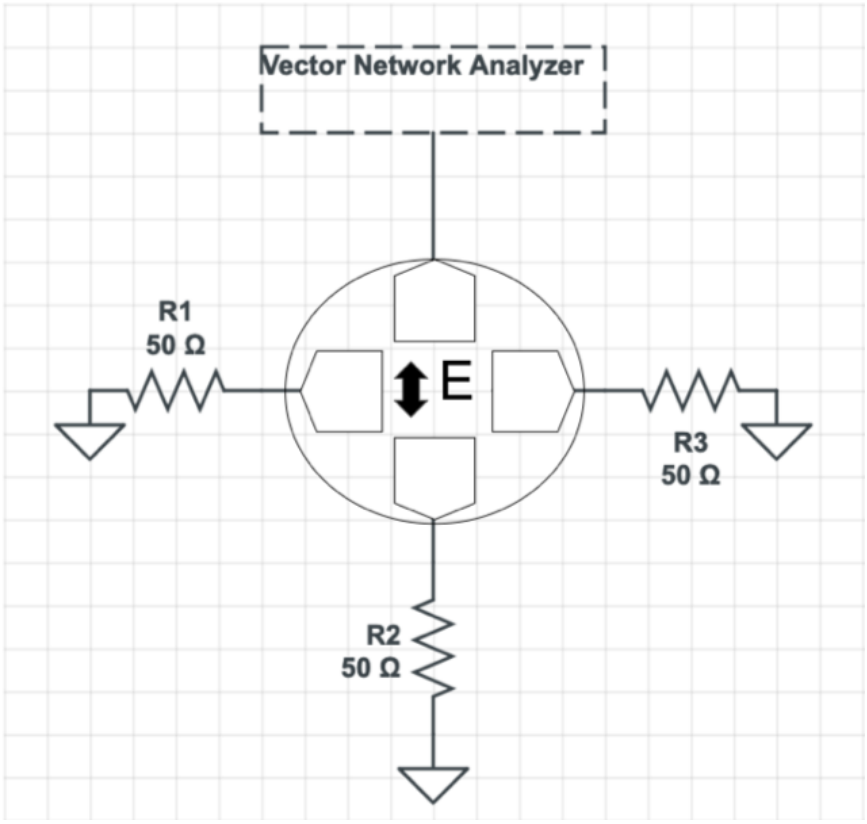

Figure 4.7: Electrical schematic of warm test readout

readout. This loss was verified by placing multiple breaks on a microstrip of different varied lengths and measuring the power at the end of each, as seen in Figure 4.8.

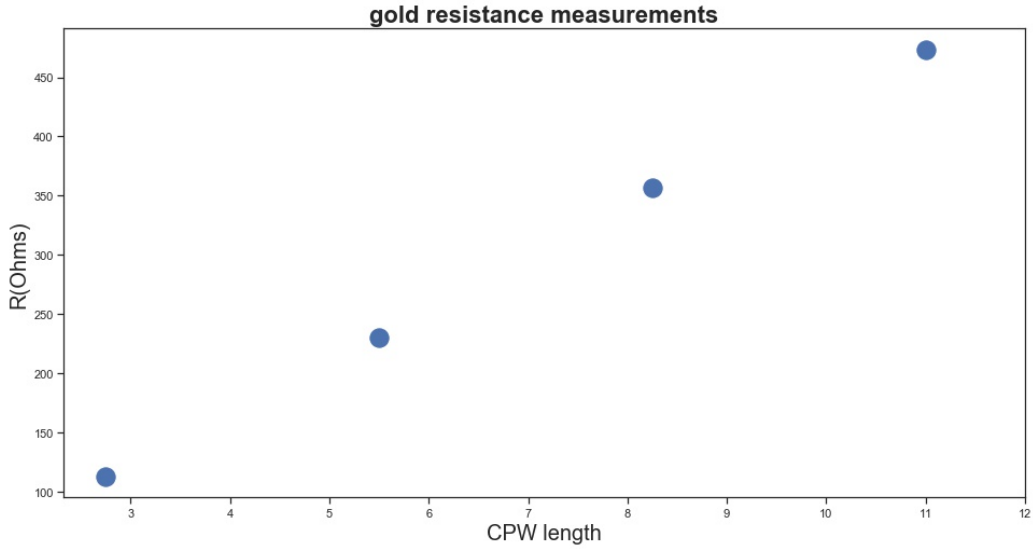

Figure 4.8: Gold resistivity at varying lengths of microstrip in millimeters.

This measurement shows us that at room temperatures, as the length of the microstrip grows, the resistance of the material increases. This indicates that the use of gold to conduct any further experiments of material loss using varied lengths of microstrips would lead to null results since the higher the resistance the lower the signal transmission through the microstrip. To verify that the signal was being absorbed by the OMT probes and not simply reflected back into the VNA, reflection and transmission measurements were taken that verified that in both pairs of terminated microstrips and the connected transmission lines there was little to no reflection as seen in Figure 4.9. In this figure we see that with the complete assembly intact and the chip in place we see absorption from the OMT probes as a dip in the signal around 100 GHz (where the probe geometry was designed to function) where in the compete assembly with no chip there is a roughly 10 dB signal reflected the entire range of frequencies.

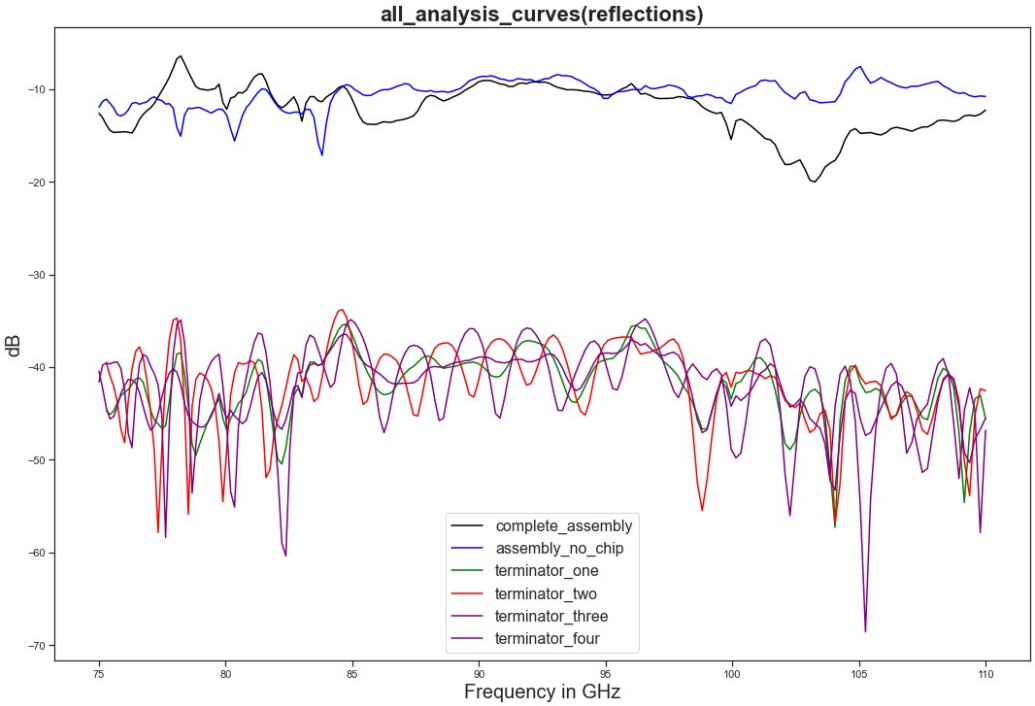

Figure 4.9: VNA reflection measurements made with complete test assembly. Complete assembly with chip and termination resistors in place (black). Complete assembly box with no chip or resistors (blue). Measured reflection of each length of microstrip (green, red, purple, maroon).

This figure also shows that when connecting the signal port to either of the microstrip lines after removing the termination, we see a massive loss in the power, indicating that the signal is unable to propagate through the microstrip either way through transmission or reflection. This pointed out a limitation in our room temperature measurements and identified the need to move on to conducting cryogenic testing of similar structures. Therefore, we then took the design and geometry of the OMT probes and applied them to our OMT test structures as described in Section 5.

4.3 Continued R&D approach

Further development and testing of these devices include the following objectives. For the mechanical mounting hardware, we use Solidworks models to design a new mechanical holder that will mount the detector wafer (Figure 4.10) in the cryostat and provide the wiring for detector bias and readout.

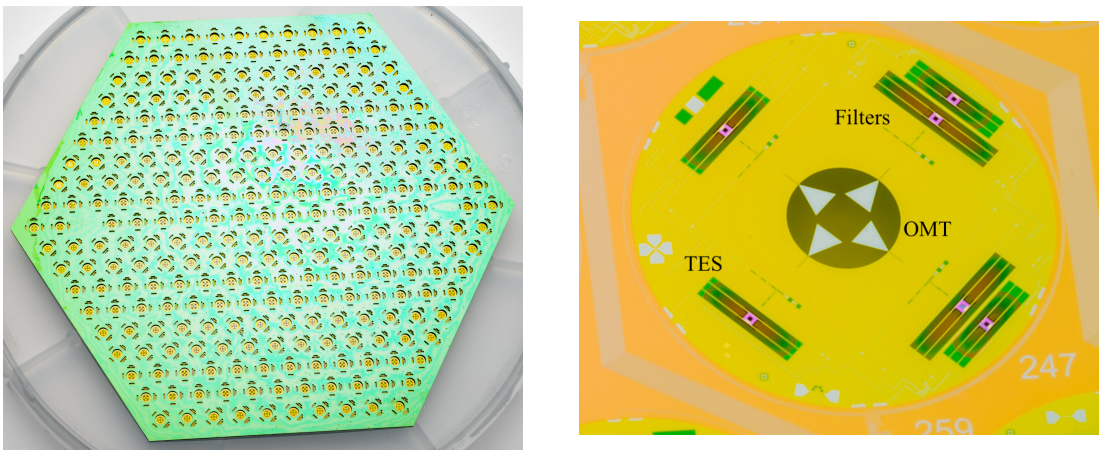

Figure 4.10: **Left:** Picture of a CMB detector array that is 150 mm across. **Right:** Close up of a single detector pixel. The signal is coupled on to the wafer from waveguide through the central OMT. The OMT also separates the signal into two orthogonal polarizations. The signal is then filtered and measured by a TES. Images courtesy Tom Cecil.

Measuring the detector I-V and R-vs-T curves, which measure the underlying physics of the detector noise, the detector saturation power, P_{sat}, which is determined by the weak thermal link and the detector operating temperature, T_c, determines the fundamental detector noise. Where the P_{sat} is measured by the detector I-V curves, the T_c on the other hand, is measured by the detector R-vs-T curves. The optical tests will involve coupling the entire wafer to a feed-horn array. We input an optical signal using either an internal blackbody source or an external source with modulated polarization. The internal black body allows us to measure the detector's optical efficiency while the external source allows us to measure the detector's polarization properties (Pan et al., 2018). We carried out these measurements and compared the results to predictions of a detector model that I will simulate using RF software, High Frequency Simulation Software (HFSS). We additionally measured the microstrip loss using different geometries and materials. These measurements were made at cryogenic temperatures in order to use Microwave Kinetic Inductance Detectors (MKIDs) as the connected detectors. These detectors were chosen because they are easier to fabricate than TES and have a faster turn-around time for the experimental stage of testing. The results of these measurements will be further discussed in Chapter 5.

4.4 Summary

In conclusion, our room temperature measurements have contributed to developing the OMT-coupled detector technology at Argonne and are part of my long-term goal of developing this technology for deployment in the CMB-S4 experiment. Next, we report on measured detector response to a black body source while cold, to measure the detector performance and efficiency that characterize the dark properties of the microstrip materials using MKIDs, which will be further discussed in Chapter 5.

CHAPTER 5

TESTING LOW-LOSS MICROSTRIP MATERIALS WITH MKIDs FOR MICROWAVE APPLICATIONS

The following work has been submitted to the Journal of Low Temperature Physics (November 1, 2021) and is reprinted below in its entirety

TESTING LOW-LOSS MICROSTRIP MATERIALS WITH MKIDs FOR MICROWAVE APPLICATIONS

J. Hood[1,2,3,4], P. S. Barry[2,3], T. Cecil[2], C. L. Chang[2,3,5], J. Li[2], S. S. Meyer[3,4,5,6], Z. Pan[3,5], E. Shirokoff[3,6], A. Tang[3,6]

[1] Dept. Physics and Astronomy, Vanderbilt University,Nashville, TN 37235

[2] Kavli Institute for Cosmological Physics, Univ. of Chicago, 5640 S. Ellis Ave., Chicago, IL 60637

[3] Argonne National Laboratory, High-Energy Physics Division, 9700 S. Cass Ave., Argonne, IL 60439

[4] Dept. of Astronomy and Astrophysics, Univ. of Chicago, 5640 S. Ellis Ave., Chicago, IL 60637

[5] Enrico Fermi Institute, Univ. of Chicago, 5640 S. Ellis Ave., Chicago, IL 60637

[6] Dept. of Physics, Univ. of Chicago, 5640 S. Ellis Ave., Chicago, IL 60637

5.1 Abstract

Future measurements of the millimeter-wavelength sky require a low-loss super- conducting microstrip, typically made from niobium and silicon-nitride, coupling the antenna to detectors. We propose a simple device for characterizing these low-loss microstrips at 150 GHz. In our device we illuminate an antenna with a thermal source and compare the measured power at 150 GHz transmitted down microstrips of different lengths. The power measurement is made using Microwave Kinetic Inductance Detectors (MKIDs) fabricated directly onto the microstrip dielectric, and comparing the measured response provides a direct measurement of the microstrip loss. Our proposed structure provides a simple device (4 layers and a DRIE etch) for characterizing the dielectric loss of various microstrip materials and substrates. We present initial results using these devices. We demonstrate that the millimeter wavelength loss of microstrip lines, a few tens of millimeters long, can be measured using a practical aluminum MKID with a black body source at a few tens of Kelvin.

5.2 Introduction

Superconducting microstrip is commonly used in detector arrays for measuring the Cosmic Microwave Background (CMB) where it serves as the transmission line for the optical signal. The CMB is an imprint of the

universe from when it was only ∼380 K years old and provides unique insight into fundamental physics. Current and upcoming measurements of the CMB temperature and polarization require large arrays of detectors observing from ∼30 GHz to 300 GHz, and superconducting microstrip is a key technology for all state-of-the-art CMB architectures as seen in (Ade et al., 2015; Suzuki et al., 2012; Posada et al., 2018; Duff et al., 2016; Rostem et al., 2012; Abazajian et al., 2016a). In this paper, we introduce a device that uses Microwave Kinetic Inductance Detectors to measure the microstrip dielectric loss at both a few GHz and ∼220 GHz. We present our device design and fabrication, a measurement of the low frequency loss for our materials, and the predicted outcome of our measurement at ∼220 GHz.

5.3 Design

Our design is shown in Fig. 5.1. Incoming light feeds our detectors via feed horns and then couples to our device through a planar ortho-mode transducer (OMT). From the OMT probes the signal travels through a Co-Planar Waveguide (CPW)-to-microstrip transition consisting of alternating sections of CPW and microstrip waveguide. The microstrip consists of a ground and top conductor layer of niobium (Nb) with a dielectric layer of silicon nitride. In each pixel, each polarization couples to two pairs of detectors where the power is split in half and transferred to the two detectors through different lengths of transmission lines. Each of the detectors are Al MKID designed with parallel plate capacitors so that they are also sensitive to the underlying dielectric and can then measure the loss at a few GHz.

5.4 Device Fabrication

Fabrication is done on a double-sided polished high resistivity 500 μm thick silicon (Si) wafer with one side coated by 450 nm of thermally grown SiO_2 and 2 μm of Low Pressure Chemical Vapor Deposition (LPCVD) Si_3N_4. These layers were both commercially deposited, the commercial Si_3N_4 layer serves as the structural support for the OMTs. The 450 nm SiO_2 layer is the etch stop layer for the deep silicon etching process Fig.5.2. The first layer of commercially deposited silicon nitride (Si_3N_4), step A (red) acts as a stop layer for the deep silicon etch done in the last step. Next, we deposit 300 nm of Nb using sputtering, which is then patterned and etched using inductively coupled plasma (ICP) etching (step B) to make the ground plane. We then grow a layer of SiN_3 with a thickness of 500 nm, which makes up the dielectric layer of our microstrip (step C). Next, a 30 nm thick layer of aluminum (Al) is subsequently deposited using sputtering, patterned, and wet etched using a standard phosphoric acid-based Al etchant (step D), which forms the Al capacitor pads and Al inductors of our MKIDs. The last metal layer consists of a 300 nm layer of Nb, which is deposited via sputtering, patterned, and plasma etched (step E). This layer makes up the Nb wiring of our device, including the CPW readout lines, OMT probes, and the CPW part of our CPW-to-microstrip transition section.

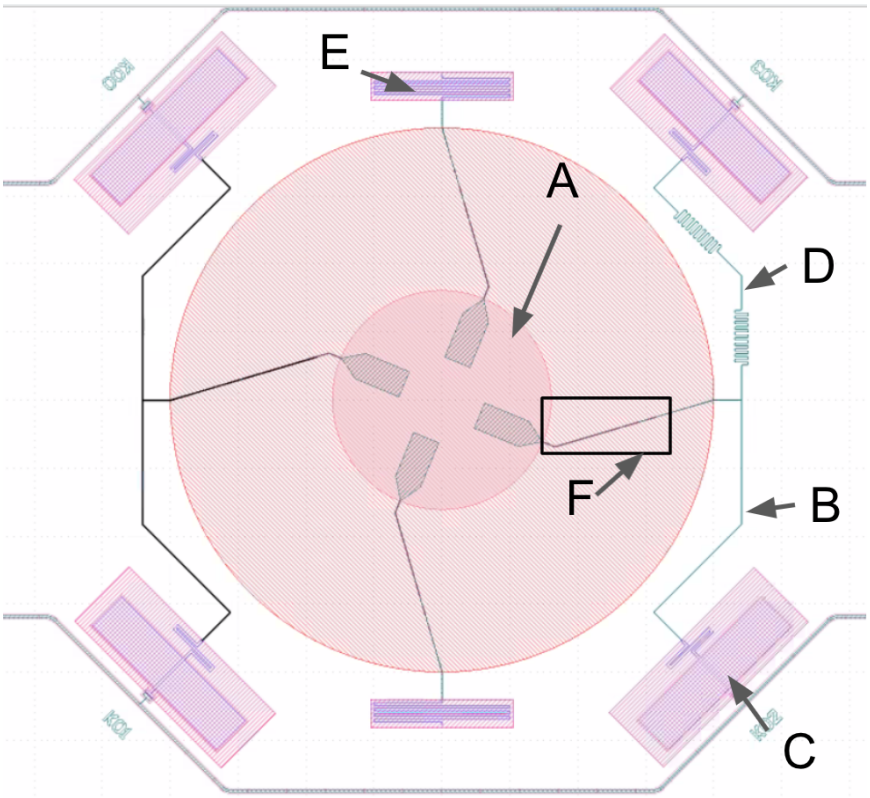

Figure 5.1: OMT with antennae probes (A), short microstrip (B) to MKID detector (C) and long microstrip (D). The long microstrip length varies across multiple devices ranging from 2.65 mm to 200 mm longer in length. Terminating resistor (E). F is the CPW to microstrip transition.

In the last step (step F), we use a deep silicon etch to remove the handle wafer from underneath the OMT and capacitor part of our MKIDs. This is done by first spinning a protective resist layer on the front surface of the wafer. We then flip the wafer, pattern the backside and use deep reactive ion etching (DRIE) to etch until the Si_3N_4 stop layer. Hydrofluoric acid (HF) bath is then used to remove the SiO_2 stop layer, which would otherwise contribute significant two-level system (TLS) loss and noise to our MKID. We also release the chip itself in this final step. The outer dimensions of the chip are defined during the deep silicon etch. We leave several tabs at the corners of the chip to physically connect it to the wafer frame during subsequent processing. After all processing is complete the chip is snapped from the wafer frame, breaking the tabs.

5.5 Testing Results

We fabricated our first batch of test devices using aluminum for both the capacitor and inductor. In Fig. 5.3 we show the S21 vs. frequency sweep measured with a vector network analyzer (VNA). There are 12 resonators in total for a yield of 100%. The resonance dip depth changes as a function of driving power at the resonator, and the bifurcation power for these resonators is around -85 dBm.

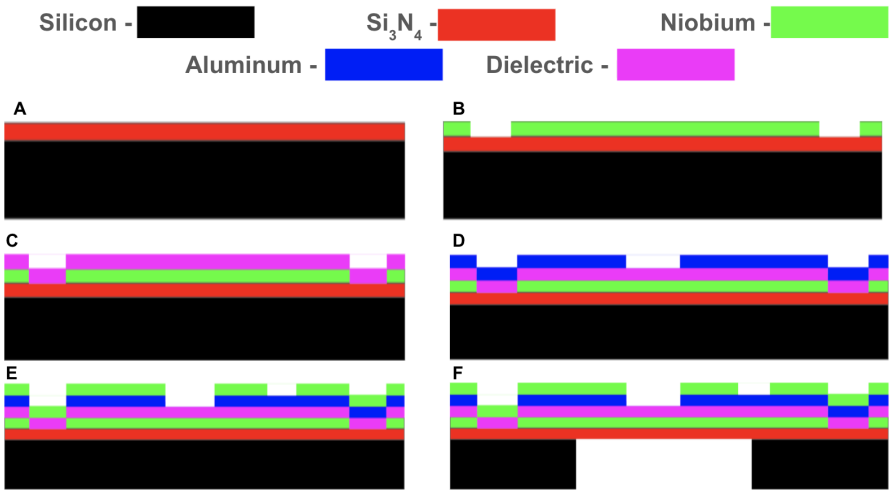

Figure 5.2: Outline of the fabrication process. The side profile shows layers of Si (black), Si_3N_4 (red), Nb (green), Al (blue), dielectric (pink). A) Si wafer with Si_3N_4 layer deposited. B) First layer of Nb. C) Dielectric layer. D) Al layer. E) Top Nb layer. F) Handle wafer etch done to open OMT window.

We measure temperature-dependent frequency shifts at high power levels as probes for dielectric loss at low frequencies below 10 GHz as described in (Carter et al., 2019). Here we measure the S21 of each resonator as a function of frequency in a small segment near the resonant frequency and fit for the resonance frequency. We then vary the stage temperature and plot the resonance frequency as a function of operating temperature. The frequency shift at lower temperatures can be described by a two-level system (TLS) model which describes the tunneling states in amorphous solids and their coupling to external electrical fields. The frequency shift is described by (Phillips, 1987; Pappas et al., 2011):

$$\frac{f(T)-f_0}{f_0} = \frac{F\delta^0_{\mathrm{TLS}}}{\pi}\left[\mathrm{Re}\Psi\left(\frac{1}{2}-\frac{f_0}{jk_BT}\right)-\log\frac{f_0}{k_BT}\right] \tag{5.1}$$

Where Ψ is the complex digamma function, F is the filling factor of the TLS, δ^0_{TLS} is the loss tangent, $f(T)$ is the temperature-dependent resonant frequency, and f_0 is the resonator frequency at zero temperature. At higher temperatures, the frequency shift is dominated by the breaking of Cooper pairs, and the model is discussed in (Gao et al., 2008). We fit the data to the model and obtained $F\delta^0_{\mathrm{TLS}} = 2\times10^{-3}$ for the resonators. The electrical field is mostly confined in the dielectric for our design, so F is close to one, and this indicates our loss tangent δ^0_{TLS} is close to 2×10^{-3}, which is typical for silicon nitride, the material we used for our dielectric. Note that the measurements done above are with a sample enclosed by an aluminum box, and this sample is not coupled to an optical source. The next step is to fabricate devices with aluminum inductors and Nb capacitors and couple the devices to an optical load.

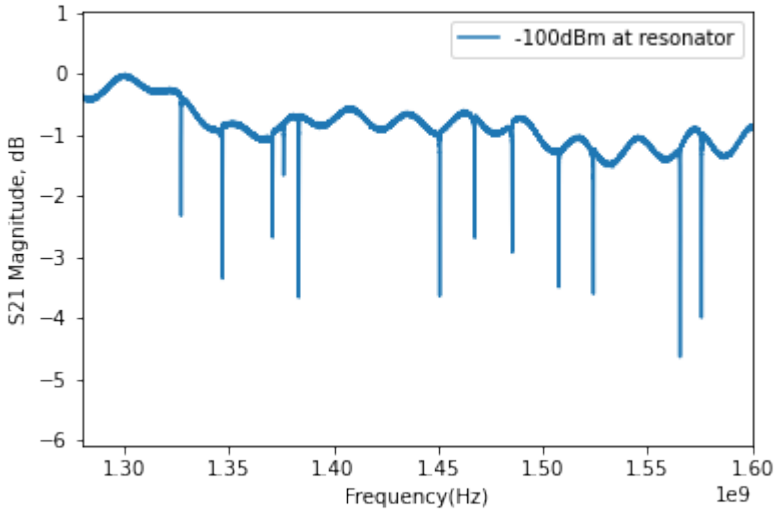

Figure 5.3: S21 vs. frequency sweep of the mm-loss device. All 12 designed resonators appear as dips with 100% yield.

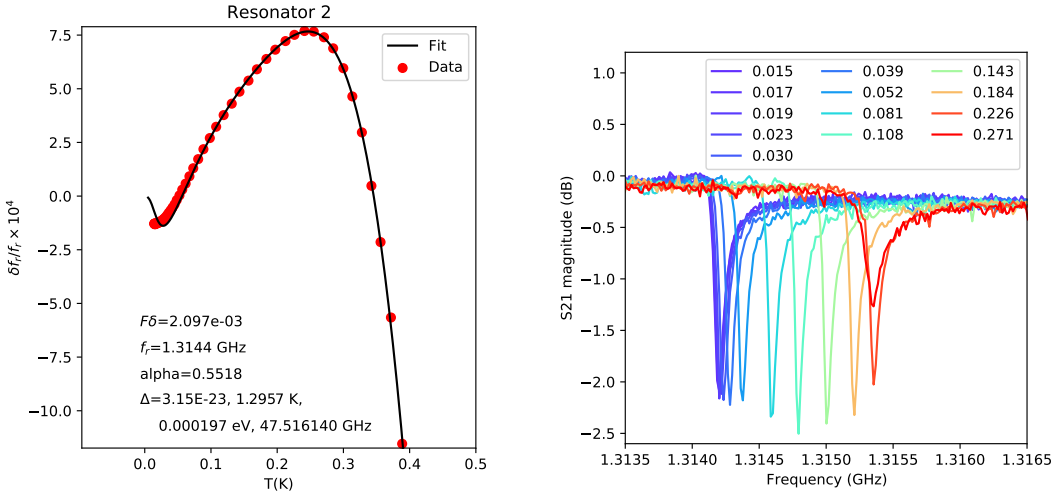

Figure 5.4: Left: the resonator fractional frequency shift as a function of temperature and the fit to Eqn. 5.1 as well as the higher-temperature model described in (Gao et al., 2008). This shows the measured loss at ∼1-10 GHz. Right: resonance S21 as a function of temperature. We extracted the resonance frequencies from the S21 measurements and fit frequency as a function of temperature.

5.6 Forecast for Microstrip-Loss Measurement at ∼ 220 GHz

In the previous section, we demonstrated that we could fabricate these devices with a 100% yield and measure the dielectric loss tangent at ∼10 GHz. We can also measure the loss at ∼220 GHz by illuminating our device with a black body and comparing the response between detectors with different lengths of transmission lines. Here, we predict the MKID optical response for varying microstrip lengths and a black body temperature

of 40 K. To model this, we first calculate the expected power that will be transmitted down the different microstrip lengths and absorbed by our detectors. Second, we calculate the number of quasiparticles generated by this absorbed power. Finally, we use our measured frequency shift as a function of temperature to convert the number of quasiparticles into the predicted detector response.

To calculate the optical power absorbed by each detector, we use the Rayleigh Jeans approximation and the following equation:

$$P = k_b * T * \Delta\nu * \eta_f^2 e^{\frac{-(d*L1)}{\lambda}} 0.5 e^{\frac{-(d*L2)}{\lambda}}, \tag{5.2}$$

where: k_b is the Boltzman constant, T is the black body temperature, $\Delta\nu$ the optical bandwidth (which we take as 25 GHz), η_f is the transmission for each of our two free space filters (which we take as 0.95), $\lambda = 7.559 \times 10^{-4}$ is the wavelength in microstrip, and L1 is the length of microstrip from the OMT paddles to the power splitter (which is $\sim$1.1 mm). There is a factor of 0.5 to account for the power splitting between the two detector arms and L2 is the varying length of microstrips (2.65 mm, 10 mm, 20 mm, 30 mm and 200 mm) and d is the dielectric loss tangent. To determine the number of quasiparticles from the absorbed optical power, we use $N_{qp} = P\tau_{qp}/\eta\Delta$. Since $\tau_{qp} \propto N_{qp}^{-1}$ as seen in (Baselmans, 2012), we are left with the following equation:

$$N_{qp}(P) = \sqrt{\frac{P\tau_{qp,0.25K}N_{qp,0.25K}}{\eta\Delta}}, \tag{5.3}$$

where $\tau_{qp,0.25K} = 0.05$ ms is the quasiparticle lifetime we measure from the our Generation Recombination (GR) noise roll-off at 250 mK, and $N_{qp,0.25K} = 595.3$ is the calculated quasiparticle number at 250 mK.

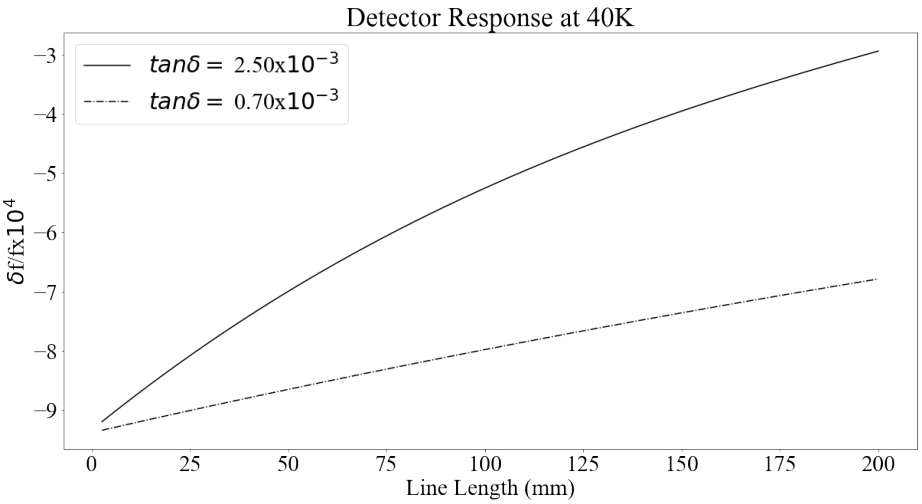

Figure 5.5: Predicted fractional frequency shift as a function of differential microstrip length at $\sim$220 GHz. Both lines are coupled to the same black body with a temperature of 40 K.

To calculate the change in detector resonance frequency due to the change in quasiparticle number, we use the slope of the high temperature data shown in Fig. **??**. Fig. 5.5 shows our prediction for the detector fractional frequency shift (δf/f) for the various microstrip lengths, a black body temperature of 40 K, and two different loss tangents. The choice of loss tangents is motivated by the measurements in the previous section and (Duff et al., 2016). Since we can typically measure δf/f down to values of 10^{-7} we expect to have no issue measuring δf/f at a level of 10^{-4}.

5.7 Summary

In conclusion, for the loss tangents that we expect these materials to have, at reasonable black body source temperatures and microstrip lengths, our predicted δf/f is large enough for us to measure the loss tangent. Therefore we have demonstrated that the mm-wavelength loss of microstrip lines, only a few tens of mm long, can be measured using a practical aluminum MKID with a black body source at a few tens of Kelvin.

CHAPTER 6

SUMMARY

In this thesis, we described the results of both microwave detector development work and our pilot AGN monitoring study. The results of our microstrip loss measurements and room temperature measurements show that for the loss tangents we expected our materials to have from previous experiments, at reasonable black body temperatures and microstrip lengths, our predicted δf/f is large enough for us to achieve measurable loss tangents. Therefore we have demonstrated that the mm-wavelength loss of microstrip lines, only a few tens of millimeters long, can be measured using a practical aluminum MKID with a black body source at a few tens of Kelvin. These measurements will help guide further efforts in the development of detector technologies for CMB experiments. Additionally, we have taken data originally meant to study the CMB and developed a method of processing it for the use of monitoring point sources. In addition to the discovery space, we have strong evidence that mm-wave monitoring of AGN will shed light on specific long-standing mysteries in AGN studies, in particular the origin of γ-ray emission and the possible correlation with high-energy neutrinos. The pilot study presented in this thesis, will serve as a great foundation for an expansion of similar software pipelines and methods to be implemented into projects like Simons Observatory and CMB-S4. Additionally, this study will serve as a catalyst to bring different astronomical communities together from different wavelength regimes, including polar and non-polar research teams to study AGN. The significance of this joint effort is that it will be able to answer questions about the emission sources of AGN through multi-wavelength correlation studies. Making the mm catalog available to everyone, as suggested by the Decadal Survey, is the most effective way to solve the long-standing questions about AGN physics.

References

Abazajian, K. N., Adshead, P., Ahmed, Z., Allen, S. W., Alonso, D., Arnold, K. S., Baccigalupi, C., Bartlett, J. G., Battaglia, N., Benson, B. A., Bischoff, C. A., Borrill, J., Buza, V., Calabrese, E., Caldwell, R., Carlstrom, J. E., Chang, C. L., Crawford, T. M., Cyr-Racine, F.-Y., Bernardis, F. D., de Haan, T., di Serego Alighieri, S., Dunkley, J., Dvorkin, C., Errard, J., Fabbian, G., Feeney, S., Ferraro, S., Filippini, J. P., Flauger, R., Fuller, G. M., Gluscevic, V., Green, D., Grin, D., Grohs, E., Henning, J. W., Hill, J. C., Hlozek, R., Holder, G., Holzapfel, W., Hu, W., Huffenberger, K. M., Keskitalo, R., Knox, L., Kosowsky, A., Kovac, J., Kovetz, E. D., Kuo, C.-L., Kusaka, A., Jeune, M. L., Lee, A. T., Lilley, M., Loverde, M., Madhavacheril, M. S., Mantz, A., Marsh, D. J. E., McMahon, J., Meerburg, P. D., Meyers, J., Miller, A. D., Munoz, J. B., Nguyen, H. N., Niemack, M. D., Peloso, M., Peloton, J., Pogosian, L., Pryke, C., Raveri, M., Reichardt, C. L., Rocha, G., Rotti, A., Schaan, E., Schmittfull, M. M., Scott, D., Sehgal, N., Shandera, S., Sherwin, B. D., Smith, T. L., Sorbo, L., Starkman, G. D., Story, K. T., van Engelen, A., Vieira, J. D., Watson, S., Whitehorn, N., and Wu, W. L. K. (2016a). Cmb-s4 science book, first edition.

Abazajian, K. N. et al. (2016b). CMB-S4 Science Book, First Edition. http://arxiv.org/abs/1610.02743/.

Abdollahi, S., Acero, F., Ackermann, M., Ajello, M., Atwood, W. B., Axelsson, M., Baldini, L., Ballet, J., Barbiellini, G., Bastieri, D., Becerra Gonzalez, J., Bellazzini, R., Berretta, A., Bissaldi, E., Blandford, R. D., Bloom, E. D., Bonino, R., Bottacini, E., Brandt, T. J., Bregeon, J., Bruel, P., Buehler, R., Burnett, T. H., Buson, S., Cameron, R. A., Caputo, R., Caraveo, P. A., Casandjian, J. M., Castro, D., Cavazzuti, E., Charles, E., Chaty, S., Chen, S., Cheung, C. C., Chiaro, G., Ciprini, S., Cohen-Tanugi, J., Cominsky, L. R., Coronado-Blázquez, J., Costantin, D., Cuoco, A., Cutini, S., D'Ammando, F., DeKlotz, M., de la Torre Luque, P., de Palma, F., Desai, A., Digel, S. W., Di Lalla, N., Di Mauro, M., Di Venere, L., Domínguez, A., Dumora, D., Fana Dirirsa, F., Fegan, S. J., Ferrara, E. C., Franckowiak, A., Fukazawa, Y., Funk, S., Fusco, P., Gargano, F., Gasparrini, D., Giglietto, N., Giommi, P., Giordano, F., Giroletti, M., Glanzman, T., Green, D., Grenier, I. A., Griffin, S., Grondin, M. H., Grove, J. E., Guiriec, S., Harding, A. K., Hayashi, K., Hays, E., Hewitt, J. W., Horan, D., Jóhannesson, G., Johnson, T. J., Kamae, T., Kerr, M., Kocevski, D., Kovac'evic', M., Kuss, M., Landriu, D., Larsson, S., Latronico, L., Lemoine-Goumard, M., Li, J., Liodakis, I., Longo, F., Loparco, F., Lott, B., Lovellette, M. N., Lubrano, P., Madejski, G. M., Maldera, S., Malyshev, D., Manfreda, A., Marchesini, E. J., Marcotulli, L., Martí-Devesa, G., Martin, P., Massaro, F., Mazziotta, M. N., McEnery, J. E., Mereu, I., Meyer, M., Michelson, P. F., Mirabal, N., Mizuno, T., Monzani, M. E., Morselli, A., Moskalenko, I. V., Negro, M., Nuss, E., Ojha, R., Omodei, N., Orienti, M., Orlando, E., Ormes, J. F., Palatiello, M., Paliya, V. S., Paneque, D., Pei, Z., Peña-Herazo, H., Perkins, J. S., Persic, M., Pesce-Rollins, M., Petrosian, V., Petrov, L., Piron, F., Poon, H., Porter, T. A., Principe, G., Rainò, S., Rando, R., Razzano, M., Razzaque, S., Reimer, A., Reimer, O., Remy, Q., Reposeur, T., Romani, R. W., Saz Parkinson, P. M., Schinzel, F. K., Serini, D., Sgrò, C., Siskind, E. J., Smith, D. A., Spandre, G., Spinelli, P., Strong, A. W., Suson, D. J., Tajima, H., Takahashi, M. N., Tak, D., Thayer, J. B., Thompson, D. J., Tibaldo, L., Torres, D. F., Torresi, E., Valverde, J., Van Klaveren, B., van Zyl, P., Wood, K., Yassine, M., and Zaharijas, G. (2020). Fermi Large Area Telescope Fourth Source Catalog. , 247(1):33.

Abitbol, M. H., Ahmed, Z., Barron, D., Thakur, R. B., Bender, A. N., Benson, B. A., Bischoff, C. A., Bryan, S. A., Carlstrom, J. E., Chang, C. L., Chuss, D. T., Crowley, K. T., Cukierman, A., de Haan, T., Dobbs, M., Essinger-Hileman, T., Filippini, J. P., Ganga, K., Gudmundsson, J. E., Halverson, N. W., Hanany, S., Henderson, S. W., Hill, C. A., Ho, S.-P. P., Hubmayr, J., Irwin, K., Jeong, O., Johnson, B. R., Kernasovskiy, S. A., Kovac, J. M., Kusaka, A., Lee, A. T., Maria, S., Mauskopf, P., McMahon, J. J., Moncelsi, L., Nadolski, A. W., Nagy, J. M., Niemack, M. D., O'Brient, R. C., Padin, S., Parshley, S. C., Pryke, C., Roe, N. A., Rostem, K., Ruhl, J., Simon, S. M., Staggs, S. T., Suzuki, A., Switzer, E. R., Tajima, O., Thompson, K. L., Timbie, P., Tucker, G. S., Vieira, J. D., Vieregg, A. G., Westbrook, B., Wollack, E. J., Yoon, K. W., Young, K. S., and Young, E. Y. (2017a). Cmb-s4 technology book, first edition.

Abitbol, M. H. et al. (2017b). CMB-S4 Technology Book, First Edition. http://arxiv.org/abs/1706.02464.

Ade, P., Aguirre, J., Ahmed, Z., Aiola, S., Ali, A., Alonso, D., Alvarez, M. A., Arnold, K., Ashton, P., Austermann, J., Awan, H., Baccigalupi, C., Baildon, T., Barron, D., Battaglia, N., Battye, R., Baxter,

E., Bazarko, A., Beall, J. A., Bean, R., Beck, D., Beckman, S., Beringue, B., Bianchini, F., Boada, S., Boettger, D., Bond, J. R., Borrill, J., Brown, M. L., Bruno, S. M., Bryan, S., Calabrese, E., Calafut, V., Calisse, P., Carron, J., Challinor, A., Chesmore, G., Chinone, Y., Chluba, J., Cho, H.-M. S., Choi, S., Coppi, G., Cothard, N. F., Coughlin, K., Crichton, D., Crowley, K. D., Crowley, K. T., Cukierman, A., D'Ewart, J. M., Dünner, R., de Haan, T., Devlin, M., Dicker, S., Didier, J., Dobbs, M., Dober, B., Duell, C. J., Duff, S., Duivenvoorden, A., Dunkley, J., Dusatko, J., Errard, J., Fabbian, G., Feeney, S., Ferraro, S., Fluxà, P., Freese, K., Frisch, J. C., Frolov, A., Fuller, G., Fuzia, B., Galitzki, N., Gallardo, P. A., Tomas Galvez Ghersi, J., Gao, J., Gawiser, E., Gerbino, M., Gluscevic, V., Goeckner-Wald, N., Golec, J., Gordon, S., Gralla, M., Green, D., Grigorian, A., Groh, J., Groppi, C., Guan, Y., Gudmundsson, J. E., Han, D., Hargrave, P., Hasegawa, M., Hasselfield, M., Hattori, M., Haynes, V., Hazumi, M., He, Y., Healy, E., Henderson, S. W., Hervias-Caimapo, C., Hill, C. A., Hill, J. C., Hilton, G., Hilton, M., Hincks, A. D., Hinshaw, G., Hložek, R., Ho, S., Ho, S.-P. P., Howe, L., Huang, Z., Hubmayr, J., Huffenberger, K., Hughes, J. P., Ijjas, A., Ikape, M., Irwin, K., Jaffe, A. H., Jain, B., Jeong, O., Kaneko, D., Karpel, E. D., Katayama, N., Keating, B., Kernasovskiy, S. S., Keskitalo, R., Kisner, T., Kiuchi, K., Klein, J., Knowles, K., Koopman, B., Kosowsky, A., Krachmalnicoff, N., Kuenstner, S. E., Kuo, C.-L., Kusaka, A., Lashner, J., Lee, A., Lee, E., Leon, D., Leung, J. S. Y., Lewis, A., Li, Y., Li, Z., Limon, M., Linder, E., Lopez-Caraballo, C., Louis, T., Lowry, L., Lungu, M., Madhavacheril, M., Mak, D., Maldonado, F., Mani, H., Mates, B., Matsuda, F., Maurin, L., Mauskopf, P., May, A., McCallum, N., McKenney, C., McMahon, J., Meerburg, P. D., Meyers, J., Miller, A., Mirmelstein, M., Moodley, K., Munchmeyer, M., Munson, C., Naess, S., Nati, F., Navaroli, M., Newburgh, L., Nguyen, H. N., Niemack, M., Nishino, H., Orlowski-Scherer, J., Page, L., Partridge, B., Peloton, J., Perrotta, F., Piccirillo, L., Pisano, G., Poletti, D., Puddu, R., Puglisi, G., Raum, C., Reichardt, C. L., Remazeilles, M., Rephaeli, Y., Riechers, D., Rojas, F., Roy, A., Sadeh, S., Sakurai, Y., Salatino, M., Sathyanarayana Rao, M., Schaan, E., Schmittfull, M., Sehgal, N., Seibert, J., Seljak, U., Sherwin, B., Shimon, M., Sierra, C., Sievers, J., Sikhosana, P., Silva-Feaver, M., Simon, S. M., Sinclair, A., Siritanasak, P., Smith, K., Smith, S. R., Spergel, D., Staggs, S. T., Stein, G., Stevens, J. R., Stompor, R., Suzuki, A., Tajima, O., Takakura, S., Teply, G., Thomas, D. B., Thorne, B., Thornton, R., Trac, H., Tsai, C., Tucker, C., Ullom, J., Vagnozzi, S., van Engelen, A., Van Lanen, J., Van Winkle, D. D., Vavagiakis, E. M., Vergès, C., Vissers, M., Wagoner, K., Walker, S., Ward, J., Westbrook, B., Whitehorn, N., Williams, J., Williams, J., Wollack, E. J., Xu, Z., Yu, B., Yu, C., Zago, F., Zhang, H., Zhu, N., and Simons Observatory Collaboration (2019). The Simons Observatory: science goals and forecasts. , 2019(2):056.

Ade, P. A. R., Aikin, R. W., Amiri, M., Barkats, D., Benton, S. J., Bischoff, C. A., Bock, J. J., Bonetti, J. A., Brevik, J. A., Buder, I., Bullock, E., Chattopadhyay, G., Davis, G., Day, P. K., Dowell, C. D., Duband, L., Filippini, J. P., Fliescher, S., Golwala, S. R., Halpern, M., Hasselfield, M., Hildebrandt, S. R., Hilton, G. C., Hristov, V., Hui, H., Irwin, K. D., Jones, W. C., Karkare, K. S., Kaufman, J. P., Keating, B. G., Kefeli, S., Kernasovskiy, S. A., Kovac, J. M., Kuo, C. L., LeDuc, H. G., Leitch, E. M., Llombart, N., Lueker, M., Mason, P., Megerian, K., Moncelsi, L., Netterfield, C. B., Nguyen, H. T., O'Brient, R., IV, R. W. O., Orlando, A., Pryke, C., Rahlin, A. S., Reintsema, C. D., Richter, S., Runyan, M. C., Schwarz, R., Sheehy, C. D., Staniszewski, Z. K., Sudiwala, R. V., Teply, G. P., Tolan, J. E., Trangsrud, A., Tucker, R. S., Turner, A. D., Vieregg, A. G., Weber, A., Wiebe, D. V., Wilson, P., Wong, C. L., Yoon, K. W., and and, J. Z. (2015). ANTENNA-COUPLED TES BOLOMETERS USED IN BICEP2,ikeck array/i, AND SPIDER. *The Astrophysical Journal*, 812(2):176.

Antonucci, R. (1993). Unified models for active galactic nuclei and quasars. , 31:473–521.

Austermann, J. E. et al. (2012). SPTpol: an instrument for CMB polarization measurements with the South Pole Telescope. *Society of Photo-Optical Instrumentation Engineers (SPIE) Conference Series*, 8452:84521E.

Ballet, J., Burnett, T. H., Digel, S. W., and Lott, B. (2020). Fermi Large Area Telescope Fourth Source Catalog Data Release 2. *arXiv e-prints*, page arXiv:2005.11208.

Baselmans, J. (2012). Kinetic inductance detectors jochem baselmans. *Journal of Low Temperature Physics*, 167(3-4):292–304.

Blandford, R., Meier, D., and Readhead, A. (2019). Relativistic Jets from Active Galactic Nuclei. *Annual Review of Astronomy and Astrophysics*, 57:467–509.

Bonning, E., Urry, C. M., Bailyn, C., Buxton, M., Chatterjee, R., Coppi, P., Fossati, G., Isler, J., and Maraschi, L. (2012). SMARTS Optical and Infrared Monitoring of 12 Gamma-Ray Bright Blazars. , 756:13.

Bonning, E. W., Bailyn, C., Urry, C. M., Buxton, M., Fossati, G., Maraschi, L., Coppi, P., Scalzo, R., Isler, J., and Kaptur, A. (2009). Correlated Variability in the Blazar 3C 454.3. , 697:L81–L85.

Carlstrom, J. E., Ade, P. A. R., Aird, K. A., Benson, B. A., Bleem, L. E., Busetti, S., Chang, C. L., Chauvin, E., Cho, H.-M., Crawford, T. M., Crites, A. T., Dobbs, M. A., Halverson, N. W., Heimsath, S., Holzapfel, W. L., Hrubes, J. D., Joy, M., Keisler, R., Lanting, T. M., Lee, A. T., Leitch, E. M., Leong, J., Lu, W., Lueker, M., Luong-van, D., McMahon, J. J., Mehl, J., Meyer, S. S., Mohr, J. J., Montroy, T. E., Padin, S., Plagge, T., Pryke, C., Ruhl, J. E., Schaffer, K. K., Schwan, D., Shirokoff, E., Spieler, H. G., Staniszewski, Z., Stark, A. A., Tucker, C., Vanderlinde, K., Vieira, J. D., and Williamson, R. (2011). The 10 Meter South Pole Telescope. , 123:568–581.

Carroll and Ostlie (2007). *An Introduction to Modern Astrophysics*.

Carter, F. W., Khaire, T., Chang, C., and Novosad, V. (2019). Low-loss single-photon NbN microwave resonators on Si. *Applied Physics Letters*, 115(9):092602.

Chang, C. L., Ade, P. A. R., Ahmed, Z., Allen, S. W., Arnold, K., Austermann, J. E., Bender, A. N., Bleem, L. E., Benson, B. A., Carlstrom, J. E., Cho, H. M., Ciocys, S. T., Cliche, J. F., Crawford, T. M., Cukierman, A., Ding, J., de Haan, T., Dobbs, M. A., Dutcher, D., Everett, W., Gilbert, A., Halverson, N. W., Hanson, D., Harrington, N. L., Hattori, K., Henning, J. W., Hilton, G. C., Holder, G. P., Holzapfel, W. L., Hubmayr, J., Irwin, K. D., Keisler, R., Knox, L., Kubik, D., Kuo, C. L., Lee, A. T., Leitch, E. M., Li, D., McDonald, M., Meyer, S. S., Montgomery, J., Myers, M., Natoli, T., Nguyen, H., Novosad, V., Padin, S., Pan, Z., Pearson, J., Posada Arbelaez, C., Reichardt, C. L., Ruhl, J. E., Saliwanchik, B. R., Simard, G., Smecher, G., Sayre, J. T., Shirokoff, E., Stark, A. A., Story, K., Suzuki, A., Thompson, K. L., Tucker, C., Vanderlinde, K., Vieira, J. D., Vikhlinin, A., Wang, G., Yefremenko, V., and Yoon, K. W. (2015). Low Loss Superconducting Microstrip Development at Argonne National Lab. *IEEE Transactions on Applied Superconductivity*, 25(3):2369231.

Chatterjee, R., Fossati, G., Urry, C. M., Bailyn, C. D., Maraschi, L., Buxton, M., Bonning, E. W., Isler, J., and Coppi, P. (2013a). An Optical-Near-infrared Outburst with no Accompanying γ-Rays in the Blazar PKS 0208-512. , 763:L11.

Chatterjee, R., Nalewajko, K., and Myers, A. D. (2013b). Implications of the Anomalous Outburst in the Blazar PKS 0208-512. , 771:L25.

Duda, J. and Bhatta, G. (2021). Gamma-ray blazar variability: new statistical methods of time-flux distributions. , 508(1):1446–1458.

Duff, S. M., Austermann, J., Beall, J. A., Becker, D., Datta, R., Gallardo, P. A., Henderson, S. W., Hilton, G. C., Ho, S. P., Hubmayr, J., Koopman, B. J., Li, D., McMahon, J., Nati, F., Niemack, M. D., Pappas, C. G., Salatino, M., Schmitt, B. L., Simon, S. M., Staggs, S. T., Stevens, J. R., Van Lanen, J., Vavagiakis, E. M., Ward, J. T., and Wollack, E. J. (2016). Advanced ACTPol Multichroic Polarimeter Array Fabrication Process for 150 mm Wafers. *Journal of Low Temperature Physics*, 184(3-4):634–641.

Dutka, M. S., Carpenter, B. D., Ojha, R., Finke, J. D., D'Ammando, F., Kadler, M., Edwards, P. G., Stevens, J., Torresi, E., Grandi, P., and et al. (2017). Multiband observations of the quasar pks 2326–502 during active and quiescent gamma-ray states in 2010–2012. *The Astrophysical Journal*, 835(2):182.

Everett, W., Ade, P. A. R., Ahmed, Z., Anderson, A. J., Austermann, J. E., Avva, J. S., Thakur, R. B., Bender, A. N., Benson, B. A., Carlstrom, J. E., Carter, F. W., Cecil, T., Chang, C. L., Cliche, J. F., Cukierman, A., Denison, E. V., de Haan, T., Ding, J., Dobbs, M. A., Dutcher, D., Foster, A., Gannon, R. N., Gilbert, A., Groh, J. C., Halverson, N. W., Harke-Hosemann, A. H., Harrington, N. L., Henning, J. W., Hilton,

G. C., Holzapfel, W. L., Huang, N., Irwin, K. D., Jeong, O. B., Jonas, M., Khaire, T., Kofman, A. M., Korman, M., Kubik, D., Kuhlmann, S., Kuo, C. L., Lee, A. T., Lowitz, A. E., Meyer, S. S., Michalik, D., Montgomery, J., Nadolski, A., Natoli, T., Nguyen, H., Noble, G. I., Novosad, V., Padin, S., Pan, Z., Pearson, J., Posada, C. M., Rahlin, A., Ruhl, J. E., Saunders, L. J., Sayre, J. T., Shirley, I., Shirokoff, E., Smecher, G., Sobrin, J. A., Stark, A. A., Story, K. T., Suzuki, A., Tang, Q. Y., Thompson, K. L., Tucker, C., Vale, L. R., Vanderlinde, K., Vieira, J. D., Wang, G., Whitehorn, N., Yefremenko, V., Yoon, K. W., and Young, M. R. (2018). Design and Bolometer Characterization of the SPT-3G First-Year Focal Plane. *Journal of Low Temperature Physics*, 193(5-6):1085–1093.

Fermi Large Area Telescope Collaboration (2021). 10-year Fermi LAT point source catalog. *The Astronomer's Telegram*, 15110:1.

Finke, J. D., Dermer, C. D., and Böttcher, M. (2008). Synchrotron self-compton analysis of tev x-ray-selected bl lacertae objects. *The Astrophysical Journal*, 686(1):181–194.

Fossati, G., Maraschi, L., Celotti, A., Comastri, A., and Ghisellini, G. (1998). A unifying view of the spectral energy distributions of blazars. *Monthly Notices of the Royal Astronomical Society*, 299(2):433–448.

Gao, J., Zmuidzinas, J., Vayonakis, A., Day, P., Mazin, B., and Leduc, H. (2008). Equivalence of the Effects on the Complex Conductivity of Superconductor due to Temperature Change and External Pair Breaking. *Journal of Low Temperature Physics*, 151(1-2):557–563.

Gebhardt, K., Bender, R., Bower, G., Dressler, A., Faber, S. M., Filippenko, A. V., Green, R., Grillmair, C., Ho, L. C., Kormendy, J., Lauer, T. R., Magorrian, J., Pinkney, J., Richstone, D., and Tremaine, S. (2000). A Relationship between Nuclear Black Hole Mass and Galaxy Velocity Dispersion. , 539:L13–L16.

Grace, E. et al. (2014). ACTPol: on-sky performance and characterization. *Society of Photo-Optical Instrumentation Engineers (SPIE) Conference Series*, 9153:915310.

Henderson, S. W. et al. (2016). Readout of two-kilopixel transition-edge sensor arrays for Advanced ACTPol. *Society of Photo-Optical Instrumentation Engineers (SPIE) Conference Series*, 9914:99141G.

Henning, J. W., Ade, P., Aird, K. A., Austermann, J. E., Beall, J. A., Becker, D., Benson, B. A., Bleem, L. E., Britton, J., Carlstrom, J. E., Chang, C. L., Cho, H.-M., Crawford, T. M., Crites, A. T., Datesman, A., de Haan, T., Dobbs, M. A., Everett, W., Ewall-Wice, A., George, E. M., Halverson, N. W., Harrington, N., Hilton, G. C., Holzapfel, W. L., Hubmayr, J., Irwin, K. D., Karfunkle, M., Keisler, R., Kennedy, J., Lee, A. T., Leitch, E., Li, D., Lueker, M., Marrone, D. P., McMahon, J. J., Mehl, J., Meyer, S. S., Montgomery, J., Montroy, T. E., Nagy, J., Natoli, T., Nibarger, J. P., Niemack, M. D., Novosad, V., Padin, S., Pryke, C., Reichardt, C. L., Ruhl, J. E., Saliwanchik, B. R., Sayre, J. T., Schaffer, K. K., Shirokoff, E., Story, K., Tucker, C., Vanderlinde, K., Vieira, J. D., Wang, G., Williamson, R., Yefremenko, V., Yoon, K. W., and Young, E. (2012). Feedhorn-coupled TES polarimeter camera modules at 150 GHz for CMB polarization measurements with SPTpol. In *Society of Photo-Optical Instrumentation Engineers (SPIE) Conference Series*, volume 8452 of .

Henning, J. W., Sayre, J. T., Reichardt, C. L., Ade, P. A. R., Anderson, A. J., Austermann, J. E., Beall, J. A., Bender, A. N., Benson, B. A., Bleem, L. E., Carlstrom, J. E., Chang, C. L., Chiang, H. C., and et al. (2018). Measurements of the temperature and e-mode polarization of the cmb from 500 square degrees of sptpol data. *The Astrophysical Journal*, 852(2):97.

Irwin, K. and Hilton, G. (2005). *Transition-Edge Sensors*, pages 63–150. Springer Berlin Heidelberg.

Ivezić, Ž., Kahn, S. M., Tyson, J. A., Abel, B., Acosta, E., Allsman, R., Alonso, D., AlSayyad, Y., Anderson, S. F., Andrew, J., Angel, J. R. P., Angeli, G. Z., Ansari, R., Antilogus, P., Araujo, C., Armstrong, R., Arndt, K. T., Astier, P., Aubourg, É., Auza, N., Axelrod, T. S., Bard, D. J., Barr, J. D., Barrau, A., Bartlett, J. G., Bauer, A. E., Bauman, B. J., Baumont, S., Bechtol, E., Bechtol, K., Becker, A. C., Becla, J., Beldica, C., Bellavia, S., Bianco, F. B., Biswas, R., Blanc, G., Blazek, J., Blandford, R. D., Bloom, J. S., Bogart, J., Bond, T. W., Booth, M. T., Borgland, A. W., Borne, K., Bosch, J. F., Boutigny, D., Brackett, C. A., Bradshaw, A., Brandt, W. N., Brown, M. E., Bullock, J. S., Burchat, P., Burke, D. L.,

Cagnoli, G., Calabrese, D., Callahan, S., Callen, A. L., Carlin, J. L., Carlson, E. L., Chandrasekharan, S., Charles-Emerson, G., Chesley, S., Cheu, E. C., Chiang, H.-F., Chiang, J., Chirino, C., Chow, D., Ciardi, D. R., Claver, C. F., Cohen-Tanugi, J., Cockrum, J. J., Coles, R., Connolly, A. J., Cook, K. H., Cooray, A., Covey, K. R., Cribbs, C., Cui, W., Cutri, R., Daly, P. N., Daniel, S. F., Daruich, F., Daubard, G., Daues, G., Dawson, W., Delgado, F., Dellapenna, A., de Peyster, R., de Val-Borro, M., Digel, S. W., Doherty, P., Dubois, R., Dubois-Felsmann, G. P., Durech, J., Economou, F., Eifler, T., Eracleous, M., Emmons, B. L., Fausti Neto, A., Ferguson, H., Figueroa, E., Fisher-Levine, M., Focke, W., Foss, M. D., Frank, J., Freemon, M. D., Gangler, E., Gawiser, E., Geary, J. C., Gee, P., Geha, M., Gessner, C. J. B., Gibson, R. R., Gilmore, D. K., Glanzman, T., Glick, W., Goldina, T., Goldstein, D. A., Goodenow, I., Graham, M. L., Gressler, W. J., Gris, P., Guy, L. P., Guyonnet, A., Haller, G., Harris, R., Hascall, P. A., Haupt, J., Hernandez, F., Herrmann, S., Hileman, E., Hoblitt, J., Hodgson, J. A., Hogan, C., Howard, J. D., Huang, D., Huffer, M. E., Ingraham, P., Innes, W. R., Jacoby, S. H., Jain, B., Jammes, F., Jee, M. J., Jenness, T., Jernigan, G., Jevremović, D., Johns, K., Johnson, A. S., Johnson, M. W. G., Jones, R. L., Juramy-Gilles, C., Jurić, M., Kalirai, J. S., Kallivayalil, N. J., Kalmbach, B., Kantor, J. P., Karst, P., Kasliwal, M. M., Kelly, H., Kessler, R., Kinnison, V., Kirkby, D., Knox, L., Kotov, I. V., Krabbendam, V. L., Krughoff, K. S., Kubánek, P., Kuczewski, J., Kulkarni, S., Ku, J., Kurita, N. R., Lage, C. S., Lambert, R., Lange, T., Langton, J. B., Le Guillou, L., Levine, D., Liang, M., Lim, K.-T., Lintott, C. J., Long, K. E., Lopez, M., Lotz, P. J., Lupton, R. H., Lust, N. B., MacArthur, L. A., Mahabal, A., Mandelbaum, R., Markiewicz, T. W., Marsh, D. S., Marshall, P. J., Marshall, S., May, M., McKercher, R., McQueen, M., Meyers, J., Migliore, M., Miller, M., Mills, D. J., Miraval, C., Moeyens, J., Moolekamp, F. E., Monet, D. G., Moniez, M., Monkewitz, S., Montgomery, C., Morrison, C. B., Mueller, F., Muller, G. P., Muñoz Arancibia, F., Neill, D. R., Newbry, S. P., Nief, J.-Y., Nomerotski, A., Nordby, M., O'Connor, P., Oliver, J., Olivier, S. S., Olsen, K., O'Mullane, W., Ortiz, S., Osier, S., Owen, R. E., Pain, R., Palecek, P. E., Parejko, J. K., Parsons, J. B., Pease, N. M., Peterson, J. M., Peterson, J. R., Petravick, D. L., Libby Petrick, M. E., Petry, C. E., Pierfederici, F., Pietrowicz, S., Pike, R., Pinto, P. A., Plante, R., Plate, S., Plutchak, J. P., Price, P. A., Prouza, M., Radeka, V., Rajagopal, J., Rasmussen, A. P., Regnault, N., Reil, K. A., Reiss, D. J., Reuter, M. A., Ridgway, S. T., Riot, V. J., Ritz, S., Robinson, S., Roby, W., Roodman, A., Rosing, W., Roucelle, C., Rumore, M. R., Russo, S., Saha, A., Sassolas, B., Schalk, T. L., Schellart, P., Schindler, R. H., Schmidt, S., Schneider, D. P., Schneider, M. D., Schoening, W., Schumacher, G., Schwamb, M. E., Sebag, J., Selvy, B., Sembroski, G. H., Seppala, L. G., Serio, A., Serrano, E., Shaw, R. A., Shipsey, I., Sick, J., Silvestri, N., Slater, C. T., Smith, J. A., Smith, R. C., Sobhani, S., Soldahl, C., Storrie-Lombardi, L., Stover, E., Strauss, M. A., Street, R. A., Stubbs, C. W., Sullivan, I. S., Sweeney, D., Swinbank, J. D., Szalay, A., Takacs, P., Tether, S. A., Thaler, J. J., Thayer, J. G., Thomas, S., Thornton, A. J., Thukral, V., Tice, J., Trilling, D. E., Turri, M., Van Berg, R., Vanden Berk, D., Vetter, K., Virieux, F., Vucina, T., Wahl, W., Walkowicz, L., Walsh, B., Walter, C. W., Wang, D. L., Wang, S.-Y., Warner, M., Wiecha, O., Willman, B., Winters, S. E., Wittman, D., Wolff, S. C., Wood-Vasey, W. M., Wu, X., Xin, B., Yoachim, P., and Zhan, H. (2019). LSST: From Science Drivers to Reference Design and Anticipated Data Products. , 873(2):111.

Kellermann, K. I., Sramek, R., Schmidt, M., Shaffer, D. B., and Green, R. (1989). VLA observations of objects in the Palomar Bright Quasar Survey. , 98:1195–1207.

Kormendy, J. and Richstone, D. (1995). Inward Bound—The Search For Supermassive Black Holes In Galactic Nuclei. , 33:581.

McMahon, J. (2004). Planar orthomode transducers for feedhorn-coupled tes polarimeters. *AIP*.

McMahon, J., Appel, J. W., Austermann, J. E., Beall, J. A., Becker, D., Benson, B. A., Bleem, L. E., Britton, J., Chang, C. L., Carlstrom, J. E., Cho, H. M., Crites, A. T., Essinger-Hileman, T., Everett, W., Halverson, N. W., Henning, J. W., Hilton, G. C., Irwin, K. D., Mehl, J., Meyer, S. S., Mossley, S., Niemack, M. D., Parker, L. P., Simon, S. M., Staggs, S. T., Visnjic, C., Wollack, E., U. -Yen, K., Yoon, K. W., and Zhao, Y. (2009). Planar Orthomode Transducers for Feedhorn-coupled TES Polarimeters. In Young, B., Cabrera, B., and Miller, A., editors, *The Thirteenth International Workshop on Low Temperature Detectors - LTD13*, volume 1185 of *American Institute of Physics Conference Series*, pages 490–493.

Meyer, M., Scargle, J. D., and Blandford, R. D. (2020). Characterizing the Gamma-Ray Variability of the Brightest Flat Spectrum Radio Quasars Observed with the Fermi LAT.

Murphy, T., Sadler, E. M., Ekers, R. D., Massardi, M., Hancock, P. J., Mahony, E., Ricci, R., Burke-Spolaor, S., Calabretta, M., Chhetri, R., de Zotti, G., Edwards, P. G., Ekers, J. A., Jackson, C. A., Kesteven, M. J., Lindley, E., Newton-McGee, K., Phillips, C., Roberts, P., Sault, R. J., Staveley-Smith, L., Subrahmanyan, R., Walker, M. A., and Wilson, W. E. (2010a). The Australia Telescope 20 GHz Survey: the source catalogue. , 402:2403–2423.

Murphy, T., Sadler, E. M., Ekers, R. D., Massardi, M., Hancock, P. J., Mahony, E., Ricci, R., Burke-Spolaor, S., Calabretta, M., Chhetri, R., de Zotti, G., Edwards, P. G., Ekers, J. A., Jackson, C. A., Kesteven, M. J., Lindley, E., Newton-McGee, K., Phillips, C., Roberts, P., Sault, R. J., Staveley-Smith, L., Subrahmanyan, R., Walker, M. A., and Wilson, W. E. (2010b). The Australia Telescope 20 GHz Survey: the source catalogue. , 402(4):2403–2423.

Pan, Z. et al. (2018). Optical characterization of the spt-3g camera. *Journal of Low Temperature Physics*, 193(3-4):305–313.

Pappas, D. P., Vissers, M. R., Wisbey, D. S., Kline, J. S., and Gao, J. (2011). Two Level System Loss in Superconducting Microwave Resonators. *IEEE Transactions on Applied Superconductivity*, 21(3):871–874.

Phillips, W. A. (1987). REVIEW ARTICLE: Two-level states in glasses. *Reports on Progress in Physics*, 50(12):1657–1708.

Planck Collaboration, Abergel, A., Ade, P. A. R., Aghanim, N., Alves, M. I. R., Aniano, G., Armitage-Caplan, C., Arnaud, M., Ashdown, M., Atrio-Barandela, F., and et al. (2014). Planck 2013 results. XI. All-sky model of thermal dust emission. , 571:A11.

Posada, C. M., Ade, P. A. R., Ahmed, Z., Anderson, A. J., Austermann, J. E., Avva, J. S., Thakur, R. B., Bender, A. N., Benson, B. A., Carlstrom, J. E., Carter, F. W., Cecil, T., Chang, C. L., Cliche, J. F., Cukierman, A., Denison, E. V., de Haan, T., Ding, J., Divan, R., Dobbs, M. A., Dutcher, D., Everett, W., Foster, A., Gannon, R. N., Gilbert, A., Groh, J. C., Halverson, N. W., Harke-Hosemann, A. H., Harrington, N. L., Henning, J. W., Hilton, G. C., Holzapfel, W. L., Huang, N., Irwin, K. D., Jeong, O. B., Jonas, M., Khaire, T., Kofman, A. M., Korman, M., Kubik, D., Kuhlmann, S., Kuo, C. L., Lee, A. T., Lowitz, A. E., Meyer, S. S., Michalik, D., Miller, C. S., Montgomery, J., Nadolski, A., Natoli, T., Nguyen, H., Noble, G. I., Novosad, V., Padin, S., Pan, Z., Pearson, J., Rahlin, A., Ruhl, J. E., Saunders, L. J., Sayre, J. T., Shirley, I., Shirokoff, E., Smecher, G., Sobrin, J. A., Stan, L., Stark, A. A., Story, K. T., Suzuki, A., Tang, Q. Y., Thompson, K. L., Tucker, C., Vale, L. R., Vanderlinde, K., Vieira, J. D., Wang, G., Whitehorn, N., Yefremenko, V., Yoon, K. W., and Young, M. R. (2018). Fabrication of Detector Arrays for the SPT-3G Receiver. *Journal of Low Temperature Physics*, 193(5-6):703–711.

Rostem, K., Bennett, C. L., Chuss, D. T., Costen, N., Crowe, E., Denis, K. L., Eimer, J. R., Lourie, N., Essinger-Hileman, T., Marriage, T. A., Moseley, S. H., Stevenson, T. R., Towner, D. W., Voellmer, G., Wollack, E. J., and Zeng, L. (2012). Detector architecture of the cosmology large angular scale surveyor. In Holland, W. S. and Zmuidzinas, J., editors, *Millimeter, Submillimeter, and Far-Infrared Detectors and Instrumentation for Astronomy VI*, volume 8452 of *Society of Photo-Optical Instrumentation Engineers (SPIE) Conference Series*, page 84521N.

Sikora, M., Begelman, M. C., and Rees, M. J. (1994). Comptonization of Diffuse Ambient Radiation by a Relativistic Jet: The Source of Gamma Rays from Blazars? , 421:153.

Sikora, M. and Madejski, G. M. (2003). Learning about Jets from Observations of Blazars. In Collin, S., Combes, F., and Shlosman, I., editors, *Active Galactic Nuclei: From Central Engine to Host Galaxy*, volume 290 of *Astronomical Society of the Pacific Conference Series*, page 287.

Sobrin, J. A., Anderson, A. J., Bender, A. N., Benson, B. A., Dutcher, D., Foster, A., Goeckner-Wald, N., Montgomery, J., Nadolski, A., Rahlin, A., Ade, P. A. R., Ahmed, Z., Anderes, E., Archipley, M., Austermann, J. E., Avva, J. S., Aylor, K., Balkenhol, L., Barry, P. S., Thakur, R. B., Benabed, K., Bianchini, F., Bleem, L. E., Bouchet, F. R., Bryant, L., Byrum, K., Carlstrom, J. E., Carter, F. W., Cecil, T. W., Chang, C. L., Chaubal, P., Chen, G., Cho, H. M., Chou, T. L., Cliche, J. F., Crawford, T. M., Cukierman, A., Daley,

C., Haan, T. d., Denison, E. V., Dibert, K., Ding, J., Dobbs, M. A., Everett, W., Feng, C., Ferguson, K. R., Fu, J., Galli, S., Gambrel, A. E., Gardner, R. W., Gualtieri, R., Guns, S., Gupta, N., Guyser, R., Halverson, N. W., Harke-Hosemann, A. H., Harrington, N. L., Henning, J. W., Hilton, G. C., Hivon, E., Holder, G. P., Holzapfel, W. L., Hood, J. C., Howe, D., Huang, N., Irwin, K. D., Jeong, O. B., Jonas, M., Jones, A., Khaire, T. S., Knox, L., Kofman, A. M., Korman, M., Kubik, D. L., Kuhlmann, S., Kuo, C. L., Lee, A. T., Leitch, E. M., Lowitz, A. E., Lu, C., Meyer, S. S., Michalik, D., Millea, M., Natoli, T., Nguyen, H., Noble, G. I., Novosad, V., Omori, Y., Padin, S., Pan, Z., Paschos, P., Pearson, J., Posada, C. M., Prabhu, K., Quan, W., Reichardt, C. L., Riebel, D., Riedel, B., Rouble, M., Ruhl, J. E., Saliwanchik, B., Sayre, J. T., Schiappucci, E., Shirokoff, E., Smecher, G., Stark, A. A., Stephen, J., Story, K. T., Suzuki, A., Tandoi, C., Thompson, K. L., Thorne, B., Tucker, C., Umilta, C., Vale, L. R., Vanderlinde, K., Vieira, J. D., Wang, G., Whitehorn, N., Wu, W. L. K., Yefremenko, V., Yoon, K. W., and Young, M. R. (2022). The Design and Integrated Performance of SPT-3G. , 258(2):42.

Sobrin, J. A., Anderson, A. J., Bender, A. N., Benson, B. A., Dutcher, D., Foster, A., Goeckner-Wald, N., Montgomery, J., Nadolski, A., Rahlin, A., Ade, P. A. R., Ahmed, Z., Anderes, E., Archipley, M., Austermann, J. E., Avva, J. S., Aylor, K., Balkenhol, L., Barry, P. S., Thakur, R. B., Benabed, K., Bianchini, F., Bleem, L. E., Bouchet, F. R., Bryant, L., Byrum, K., Carlstrom, J. E., Carter, F. W., Cecil, T. W., Chang, C. L., Chaubal, P., Chen, G., Cho, H.-M., Chou, T.-L., Cliche, J.-F., Crawford, T. M., Cukierman, A., Daley, C., Haan, T. d., Denison, E. V., Dibert, K., Ding, J., Dobbs, M. A., Everett, W., Feng, C., Ferguson, K. R., Fu, J., Galli, S., Gambrel, A. E., Gardner, R. W., Gualtieri, R., Guns, S., Gupta, N., Guyser, R., Halverson, N. W., Harke-Hosemann, A. H., Harrington, N. L., Henning, J. W., Hilton, G. C., Hivon, E., Holder, G. P., Holzapfel, W. L., Hood, J. C., Howe, D., Huang, N., Irwin, K. D., Jeong, O. B., Jonas, M., Jones, A., Khaire, T. S., Knox, L., Kofman, A. M., Korman, M., Kubik, D. L., Kuhlmann, S., Kuo, C.-L., Lee, A. T., Leitch, E. M., Lowitz, A. E., Lu, C., Meyer, S. S., Michalik, D., Millea, M., Natoli, T., Nguyen, H., Noble, G. I., Novosad, V., Omori, Y., Padin, S., Pan, Z., Paschos, P., Pearson, J., Posada, C. M., Prabhu, K., Quan, W., Reichardt, C. L., Riebel, D., Riedel, B., Rouble, M., Ruhl, J. E., Saliwanchik, B., Sayre, J. T., Schiappucci, E., Shirokoff, E., Smecher, G., Stark, A. A., Stephen, J., Story, K. T., Suzuki, A., Tandoi, C., Thompson, K. L., Thorne, B., Tucker, C., Umilta, C., Vale, L. R., Vanderlinde, K., Vieira, J. D., Wang, G., Whitehorn, N., Wu, W. L. K., Yefremenko, V., Yoon, K. W., and Young, M. R. (2022). The Design and Integrated Performance of SPT-3G. *The Astrophysical Journal Supplement Series*, 258(2):42. Publisher: American Astronomical Society.

Story, K. T., Reichardt, C. L., Hou, Z., Keisler, R., Aird, K. A., Benson, B. A., Bleem, L. E., Carlstrom, J. E., Chang, C. L., Cho, H. M., Crawford, T. M., Crites, A. T., de Haan, T., Dobbs, M. A., Dudley, J., Follin, B., George, E. M., Halverson, N. W., Holder, G. P., Holzapfel, W. L., Hoover, S., Hrubes, J. D., Joy, M., Knox, L., Lee, A. T., Leitch, E. M., Lueker, M., Luong-Van, D., McMahon, J. J., Mehl, J., Meyer, S. S., Millea, M., Mohr, J. J., Montroy, T. E., Padin, S., Plagge, T., Pryke, C., Ruhl, J. E., Sayre, J. T., Schaffer, K. K., Shaw, L., Shirokoff, E., Spieler, H. G., Staniszewski, Z., Stark, A. A., van Engelen, A., Vanderlinde, K., Vieira, J. D., Williamson, R., and Zahn, O. (2013). A Measurement of the Cosmic Microwave Background Damping Tail from the 2500-Square-Degree SPT-SZ Survey. , 779(1):86.

Suzuki, A., Arnold, K., Edwards, J., Engargiola, G., Ghribi, A., Holzapfel, W., Lee, A. T., Meng, X. F., Myers, M. J., O'Brient, R., Quealy, E., Rebeiz, G., Richards, P., Rosen, D., and Siritanasak, P. (2012). Multichroic dual-polarization bolometric detectors for studies of the cosmic microwave background. In Holland, W. S. and Zmuidzinas, J., editors, *Millimeter, Submillimeter, and Far-Infrared Detectors and Instrumentation for Astronomy VI*, volume 8452 of *Society of Photo-Optical Instrumentation Engineers (SPIE) Conference Series*, page 84523H.

Urry, C. M. and Padovani, P. (1995). Unified Schemes for Radio-Loud Active Galactic Nuclei. , 107:803.

Urry, C. M. and Padovani, P. (1995). Unified Schemes for Radio-Loud Active Galactic Nuclei. *Pasp*, 107:803.

Welsh, W. F. (1999). On the Reliability of Cross-Correlation Function Lag Determinations in Active Galactic Nuclei. , 111(765):1347–1366.

CHAPTER 7

APPENDIX

Table 7.1: AGN found in AT20G and SPTpol survey, decreasing in average SPT flux

RA	DEC	AT20G Flux (mJy)	SPTpol Flux (mJy)
352.33206	-49.92615	221	857.6891
14.69086	-56.98399	842	733.0095
12.49499	-57.63815	1872	495.0398
331.92767	-53.77746	1122	443.1507
339.79593	-57.02045	925	395.8309
348.93268	-50.31010	726	369.616
15.886239	-64.6495	323	311.6593
354.04837	-52.60524	1069	281.158
353.685	-52.854459	934	279.93
23.26988	-51.99899	1198	227.9214
19.95725	-53.953169	245	204.966
340.77765	-62.849219	235	189.4486
341.56573	-56.13224	1052	176.9112
28.57927	-51.12897	329	170.75
21.23532	-51.219	745	143.0875
337.78384	-62.52101	275	130.4427
15.54022	-56.61524	204	125.5117
359.68448	-60.88035	311	117.8467
357.10141	-60.82291	144	116.7781
347.2583	-50.84908	135	112.43
356.8309	-51.17595	407	111.982
26.700029	-52.04054	226	110.5314
354.3598	-59.02013	264	104.169
25.60351	-57.4985	75	100.8344
345.39951	-59.222519	155	95.2117
355.86041	-56.43956	109	89.5304
330.99731	-61.504059	387	89.3338
343.7359	-59.43315	180	88.2769
2.00597	-52.72435	124	88.1281
4.85861	-56.69463	72	86.6067
345.96402	-54.1123	206	85.7667
22.07921	-56.82579	189	84.5478
0.71924	-59.8039	71	81.4112
17.30534	-60.828369	460	79.4477
26.05917	-64.36068	186	76.3292
332.199039	-63.428769	353	72.9623
5.92585	-59.50798	85	67.0503
358.91449	-54.3089	93	64.9062
17.55952	-63.26379	206	63.7246
15.30378	-62.5502	184	58.325
5.75459	-56.83405	99	57.3348
350.19791	-53.16189	79	55.7061

Continued on next page

Table 7.1: *(Continued)*AGN found in AT20G and SPTpol survey, decreasing in average SPT flux

RA	DEC	AT20G Flux (mJy)	SPTpol Flux (mJy)
14.72664	-52.32257	170	55.0059
359.94571	-50.70908	68	54.1629
24.95505	-52.29552	91	53.8353
15.77591	-51.151959	82	52.6971
14.27087	-52.23793	97	52.4791
7.89025	-51.7224	78	51.7095
333.39017	-63.49933	316	49.697
29.20482	-54.66137	278	47.8283
339.59885	-51.24187	54	46.0396
338.58746	-54.10189	80	44.9852
21.97799	-51.61019	100	44.9567
349.31079	-62.258109	132	44.8609
343.58746	-51.81415	56	44.6636
28.49135	-54.113319	50	44.5732
1.82629	-61.2165	150	43.8109
3.6067	-56.63743	134	42.5683
0.76231	-55.501619	44	42.3707
355.820979	-57.16091	127	41.8845
4.69814	-51.24754	154	40.3085
5.63718	-51.88686	77	40.1167
350.24872	-54.0427	87	39.1415
339.76801	-55.434059	152	38.7845
350.424679	-64.63515	62	37.8657
340.59256	-60.74119	66	37.5519
350.71716	-53.367419	130	37.1451
1.48773	-56.47314	151	36.215
342.14145	-59.567869	57	35.8419
0.78995	-54.747869	95	35.758
16.02771	-56.95244	40	35.3449
23.947879	-52.73672	55	34.6265
14.83002	-61.44543	70	33.8022
10.02401	-59.062969	174	33.7057
9.39596	-53.12544	81	33.5737
12.27224	-55.35252	89	33.5723
354.34491	-52.27124	221	32.7358
330.71362	-56.59536	69	32.571
15.87355	-51.596709	87	31.433
343.95596	-52.76189	247	30.7714
1.05539	-52.9166	65	30.2956
358.34286	-58.95704	62	29.715
25.42046	-56.84158	135	28.8379
23.5335	-55.43769	47	28.5584
331.81226	-63.42705	76	27.6372
2.40043	-63.95921	59	27.2022
21.5964	-51.050979	111	27.0822
349.81647	-53.53011	75	26.7883
356.96692	-59.262069	72	26.5597
28.78945	-64.42266	51	26.1764

Continued on next page

Table 7.1: *(Continued)*AGN found in AT20G and SPTpol survey, decreasing in average SPT flux

RA	DEC	AT20G Flux (mJy)	SPTpol Flux (mJy)
25.72907	-60.74803	106	25.6922
336.7774	-52.33105	152	25.4988
6.29199	-54.45881	59	25.0504
332.56216	-50.5175	51	22.6796
347.75281	-60.756159	47	22.5762
337.67654	-63.4906	103	22.433
340.96518	-56.93965	142	22.1428
357.18481	-58.78605	48	22.0438
342.90076	-54.88641	62	21.7274
23.9187	-51.82798	60	21.4474
356.17227	-61.14048	90	21.3408
27.70516	-60.73354	48	21.2709
337.54202	-63.17834	165	20.9919
2.34176	-51.50249	49	20.9789
352.01886	-56.50138	43	20.874
334.60229	-64.91107	71	20.5517
332.62671	-55.14559	64	20.3353
348.36017	-53.724909	139	19.8179
20.41382	-63.15081	54	19.7166
29.340359	-54.3767	48	19.6784
340.07059	-52.531169	55	19.5101
22.13795	-52.92033	175	19.3522
3.3499	-50.08538	71	18.9308
334.92569	-52.90662	90	18.9242
334.57794	-50.64648	119	17.871
9.35586	-59.29803	50	17.695
334.17035	-56.62517	64	17.6404
15.95425	-63.84885	61	17.4556
355.32568	-58.26928	204	17.3142
337.67053	-54.25526	57	17.2036
351.29456	-56.941759	121	16.0752
20.02916	-52.1834	59	15.7316
347.01578	-52.315	72	15.3273
9.55393	-61.21159	68	15.242
349.21924	-55.13178	104	15.1697
347.789029	-56.41394	99	14.7126
342.90698	-58.019969	79	14.6078
18.33923	-53.49431	117	14.4342
336.73737	-62.63039	84	14.0324
6.9038	-54.152359	43	13.7389
11.33271	-54.79409	62	13.721
347.61609	-59.6834	134	13.502
334.96887	-63.55955	75	13.1115
334.09488	-52.6313	82	13.041
0.79948	-59.097019	49	12.9605
343.48816	-50.420629	60	12.9207
4.98646	-62.883419	42	12.7752
6.304559	-60.47472	52	12.5526

Continued on next page

Table 7.1: *(Continued)*AGN found in AT20G and SPTpol survey, decreasing in average SPT flux

RA	DEC	AT20G Flux (mJy)	SPTpol Flux (mJy)
344.188479	-51.97893	157	11.8937
25.38427	-54.46337	43	11.6725
347.48892	-61.141319	87	10.8226
12.27283	-64.4197	94	10.7395
0.7247	-56.35423	94	10.6559
5.83467	-60.77194	47	10.6526
4.00498	-63.16757	67	10.2283
336.75638	-52.557269	110	9.977
28.985409	-51.42559	115	9.6648
341.37305	-59.92252	71	9.1708
345.49658	-53.72638	86	9.1062
20.29263	-56.043269	50	8.85
14.683639	-59.53086	50	8.4863
331.26648	-55.298269	92	7.4575
3.3216	-56.17326	48	7.4517
354.8027	-55.3928	65	7.2478
344.74728	-59.32861	42	6.925
354.338989	-50.557	48	6.6134
348.28159	-55.06641	61	6.4576
22.9591	-51.86458	49	6.4218
16.56182	-50.73233	47	6.3053
350.53409	-54.7567	73	6.0491
341.78333	-54.15028	56	5.617